Sexual coordination in a whole-brain map of prairie-vole pair-bonding

Morgan L. Gustison,[1] Rodrigo Muñoz Castañeda,[2] Pavel Osten,[2*] Steven M. Phelps [1,3*]

[1] Department of Integrative Biology, The University of Texas at Austin; Austin, TX, USA

[2] Cold Spring Harbor Laboratory; Cold Spring Harbor, NY, USA

[3] Institute for Neuroscience, The University of Texas at Austin; Austin, TX, USA

* Corresponding authors

Steven Phelps, UT Austin, sphelps@utexas.edu

Pavel Osten, CSHL, osten@cshl.edu

Abstract: Sexual bonds are central to the social lives of many species, including humans, and monogamous prairie voles have become the predominant model for investigating such attachments. We developed an automated whole-brain mapping pipeline to identify brain circuits underlying pair-bonding behavior. We identified bonding-related c-Fos induction in 68 brain regions clustered in seven major brain-wide neuronal circuits. These circuits include known regulators of bonding, such as the bed nucleus of the stria terminalis, paraventricular hypothalamus, ventral pallidum, and prefrontal cortex. They also include brain regions previously unknown to shape bonding, such as ventromedial hypothalamus, medial preoptic area and the medial amygdala, but that play essential roles in bonding-relevant processes, such as sexual behavior, social reward and territorial aggression. Contrary to some hypotheses, we found that circuits active during mating and bonding were largely sexually monomorphic. Moreover, c-Fos induction across regions was strikingly consistent between members of a pair, with activity best predicted by rates of ejaculation. A novel cluster of regions centered in the amygdala remained coordinated after bonds had formed, suggesting novel substrates for bond maintenance. Our tools and results provide an unprecedented resource for elucidating the networks that translate sexual experience into an enduring bond.

Introduction

Bonds are essential to the social lives of many species, enabling individuals to coordinate parental care, territorial defense, or other shared activities (Emlen & Oring, 1977; Marlowe, 2000; Trivers, 1972). Among humans, friendships and a happy marriage protect against a wide range of stressors and their sequelae (Baumeister & Leary, 1995; Hawkley & Cacioppo, 2010), while social integration is one of the strongest predictors of reduced morbidity and mortality risk (Snyder-Mackler et al., 2020). Recent evidence suggests social buffering against stress-related disease can be found in many other mammals as well, including species of nonhuman primates, rodents, ungulates, and hyrax (Snyder-Mackler et al., 2020). Nonhuman animals offer unique insights into the mechanisms of social attachment and their consequences.

The neurobiology of bonding is most studied in the prairie vole, a socially monogamous rodent in which males and females form bonds, share a nest, and raise young together (Lieberwirth & Wang, 2014; L. J. Young & Wang, 2004). In prairie voles, as in many pair-bonding species, bonds form in response to courtship and repeated mating (Carter et al., 1995; Getz et al., 1993); indeed, copulation itself is regarded as a form of courtship that allows mutual assessment and coordinates reproduction (Dewsbury, 1988; Eberhard, 1996). Because of these characteristics, prairie voles have become an excellent model species to study neural circuits that underpin affiliative behaviors (Kenkel et al., 2021). Classic studies emphasized the roles of neuropeptides in reward circuitry (Aragona et al., 2006; L. J. Young & Wang, 2004), work that has been refined to reveal that neural ensembles in the nucleus accumbens encode approach behavior between mates (Scribner et al., 2020), and the strength of functional connections between nucleus accumbens and prefrontal cortex predicts social contact (Amadei et al., 2017). Mated prairie voles exhibit empathy-like consolation behavior that reduces markers of distress in both members of a pair (Burkett et al., 2016). In one common model, some 18 different brain regions shape aspects of memory, reward and approach that are essential to bond formation and its consequences (Walum & Young, 2018). Despite this extraordinary work, we still have an incomplete understanding of the circuits that enable the experience of mating to become an

enduring bond. Building upon this foundation will require a shift from a piece-meal to systems-wide perspective.

In several species, including wasps, fish, bats, mice, and humans, researchers using a variety of biological measures find that social interactions are accompanied by coordinated neural states (Hasson et al., 2012; Kingsbury et al., 2019; Kinreich et al., 2017; Long et al., 2020; Vu et al., 2020; Zhang & Yartsev, 2019). In fighting fish (*Betta splendens*) and paper wasps (*Polistes fuscatus*), shared brain-transcriptomic signatures occur in individuals immediately after competitive interactions (Uy et al., 2021; Vu et al., 2020). In Egyptian fruit bats (*Rousettus aegyptiacus*) and lab mice, freely interacting individuals have correlated neural activity in the frontal cortex, and increases in inter-brain correlations predict whether subsequent interactions occur (Kingsbury et al., 2019; Zhang & Yartsev, 2019). In humans, inter-brain EEG recordings become synchronized in a variety of interactive contexts (Hasson et al., 2012), such as during social gaze and positive affect in couples (Kinreich et al., 2017). Such data have led to the inference that closely interacting dyads, including bonded individuals, coordinate aspects of their physiological and neural states (Long et al., 2020).

In contrast to the emphasis on shared brain states, sex differences in neuroendocrine mechanisms mean that not only are behaviors often sexually dimorphic, but even if the sexes exhibit similar behaviors, a baseline difference in brain function may require distinct behavioral mechanisms (de Vries, 2004). In the monogamous oldfield mouse, *Peromyscus polionotus*, for example, genome-wide association studies implicate different mechanisms in the regulation of male and female parental care (Bendesky et al., 2017). The “dual function hypothesis” has suggested that similarly dimorphic mechanisms may underlie bonding or parental behaviors more generally (de Vries, 2004). To understand attachment, it is essential to examine neural function across the entire brain (López-Gutiérrez et al., 2021; Yee et al., 2016), and to explore individual and sex differences in such circuits as bonds form.

To systematically examine the mechanisms of pair bond formation, we developed a whole-brain imaging and computational analysis pipeline that includes the first 3D histological atlas of the prairie-vole brain. This atlas and analysis pipeline enables the high-throughput, automated counting of cell markers throughout the prairie-vole brain. We used this tool to test for sexual dimorphism in the structure of prairie-vole brains, and to compare the gross anatomy

of the prairie-vole brain to the laboratory mouse. In order to map regions and circuits active during bonding, we next quantified immediate-early gene (IEG) induction in 824 brain regions at key times in bond formation. This represents the first unbiased identification of circuits active during bonding. Doing so allowed us to examine how the experience of mating finds its way into bonding circuits. It also allowed us to rigorously test two alternative hypotheses: that mating and bonding promote coordinated changes in the brains of mated pairs; and conversely, that sexually dimorphic circuits underlie bonding in males and females.

Results

A novel whole-brain imaging pipeline for the prairie vole

We began by generating a common coordinate framework (CCF) for the prairie-vole brain by iteratively averaging tissue autofluorescence from 191 brains imaged using light-sheet fluorescence microscopy (LSFM). Each of the brains were co-registered into this coordinate framework for computational analyses (Methods). Next, we registered an LSFM-based CCF of the mouse brain onto the prairie-vole CCF, enabling us to apply anatomical labels of the Allen Reference Atlas (ARA; Figure 1A, Figure Supplement 1a, and Video 1) (Dong, 2008). This alignment revealed that the prairie-vole brain is ~30% larger than the mouse brain and distinct in shape (Figure 1A), but that relative volumes of brain regions were consistent across species and showed no evidence of sexual dimorphism (Figure Supplement 1a, Supplemental Files 1 and 2).

To validate and refine the ARA anatomical borders in the prairie-vole brain, we performed whole-brain Nissl staining as well as iDISCO immuno-labelling targeting the cell-specific markers tyrosine hydroxylase (TH), parvalbumin (PV) and somatostatin (SST); we then aligned these images onto the prairie-vole CCF (Figure 1B,C and Figure Supplement 1a). Lastly, we adapted for the prairie vole our computational pipeline for whole-brain detection and statistical comparisons of c-Fos+ neurons in LSFM-imaged brains (Kim et al., 2015, 2016; Renier et al., 2016) (Figure 1C). With a robust atlas and analysis tools in place, we conducted a detailed study of the time-course of mating and bond formation to examine IEG induction across the prairie-vole brain and test our hypotheses.

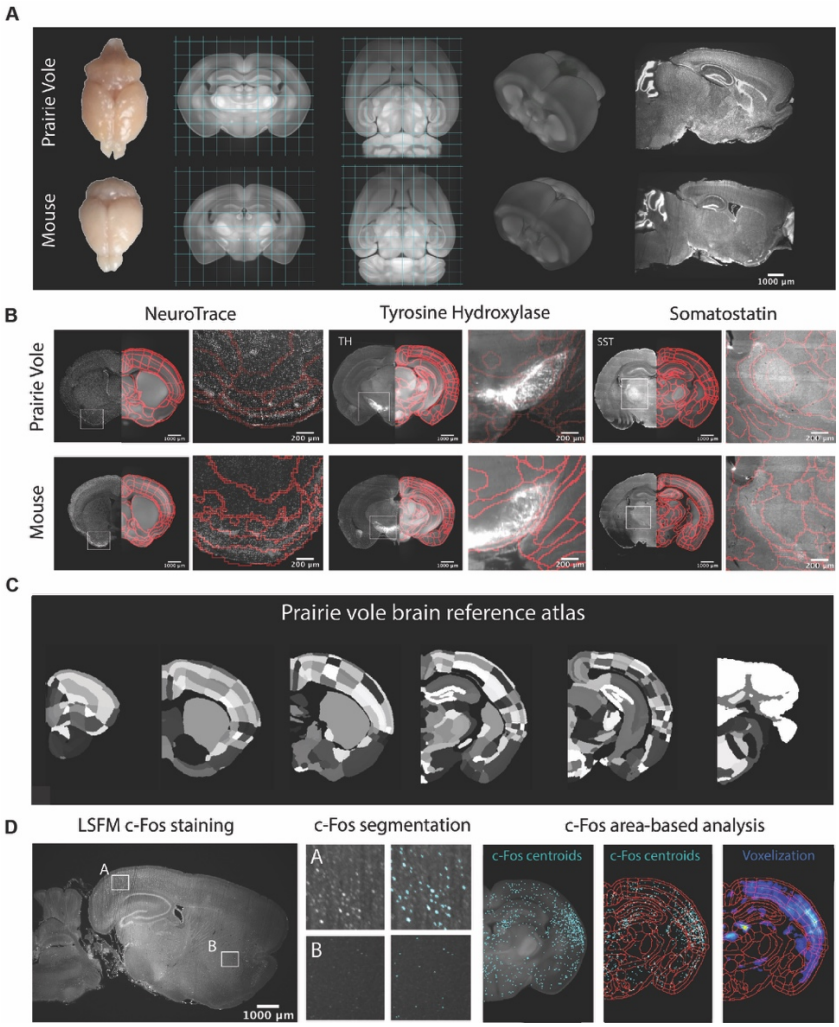

Figure 1. Prairie vole reference brain and atlas generation for automatic c-Fos analysis. (A) Generation of prairie vole (upper row) and mouse (lower row) reference brains using LSFM imaging. Top view of both prairie vole and mouse brains after perfusion. Cross-section of a coronal and horizontal views of prairie vole and mouse reference brains built after the co-registration of ~200 brains per species. Prairie vole whole brain is 1.39 times bigger than the mouse (see Figure Supplement 1 and Supplemental File 1). 3D renderization of both prairie vole and mouse brains. Sagittal view of prairie vole and mouse whole brain fluorescent Nissl (NeuroTrace) staining imagined with LSFM. **(B)** Whole brain staining of both prairie vole (upper row) and mouse (lower row) brains registered to the reference brain. In red, boundaries of registered mouse reference atlas onto both prairie vole and mouse reference brains. NeuroTrace, TH and SST were registered and overlay to the atlases for validation. **(C)** Coronal sections of resulting prairie vole atlas after manual validation. **(D)** Overview of LSFM prairie vole c-Fos+ analysis pipeline. (left panel) Sagittal section of prairie vole c-Fos immunolabeling and imaged with LSFM. (center panel) Detail of two brain locations immunolabeled with c-Fos and overlay with resulting segmentation. (right panel) Area-based analysis of c-Fos+ cells. All c-Fos+ cells centroids are registered to the prairie vole reference brain and analyzed using the new prairie vole reference atlas. For each brain it is generated a voxelized representation of all c-Fos+ cells in the same prairie vole reference space and overlay with the reference atlas.

Pair-bonding involves a dynamic repertoire of social interactions

Sexually responsive voles typically mate within the first hour of pairing, and repeated mating over ~6h initiates partner preferences characteristic of attachment (DeVries & Carter, 1999). The bond stabilizes between ~12-24h, leading to prolonged changes in attachment and related behaviors (DeVries & Carter, 1999; Williams et al., 1992). With these milestones in mind, we precisely manipulated mating experience and examined how repeated sexual behaviors lead to a bond (Figure 2A, Figure S2a-d, Supplemental File 3).

To coordinate the timing of mating, all subjects were isolated for 4-5 days, females were brought into estrus, and both sexes were screened for sexual receptivity (see Figure 2A). Subjects assigned to the bonding condition were paired with a novel opposite-sexed individual; to control for non-sexual social affiliation, remaining subjects were re-paired with a familiar same-sex sibling. Members of each pair were isolated on either side of a divider for 2h. Following this acclimation, the divider was removed, and the pair could interact freely. (Figure 2A). Behavior sessions were terminated following a fixed timeline: animals were euthanized just before barrier removal (0h), following initial mating (2.5h), after initial bond formation (6h), or after bond stabilization (22h). Automated behavioral measures, such as proximity, vocalization, and relative movement were scored throughout the behavioral sessions. We performed detailed manual scoring for 1h focal intervals beginning 2h before euthanasia – a timeframe that reveals the behavioral states of animals during IEG induction (Figure 2B-C, Figure Supplement 2a-e, and Supplemental File 3).

Mate and sibling pairs did not differ in locomotor activity or time spent in side-by-side contact ("huddling"; t-tests, FDR-corrected q=0.17 and 0.37; Figure 2D). Mate pairs progressed through known stages of mating behavior, showing elevated rates of anogenital investigation and vocalization (t-tests, q=0.0003 and q=0.0003); males moved more often toward females, while females moved away from their partners (paired t-test, q=0.01), a behavior consistent with female copulatory pacing (Pfaus et al., 2001). Consummatory aspects of mating – mounting, intromission and ejaculation – were common in both the 2.5h and 6h focal windows; by 22h mating was rare, and levels of male-female huddling resembled those of same-sex siblings housed together since birth (Figure 2E). This profile is consistent with literature on the timing and process of prairie vole bond formation (DeVries & Carter, 1999; Williams et al., 1992).

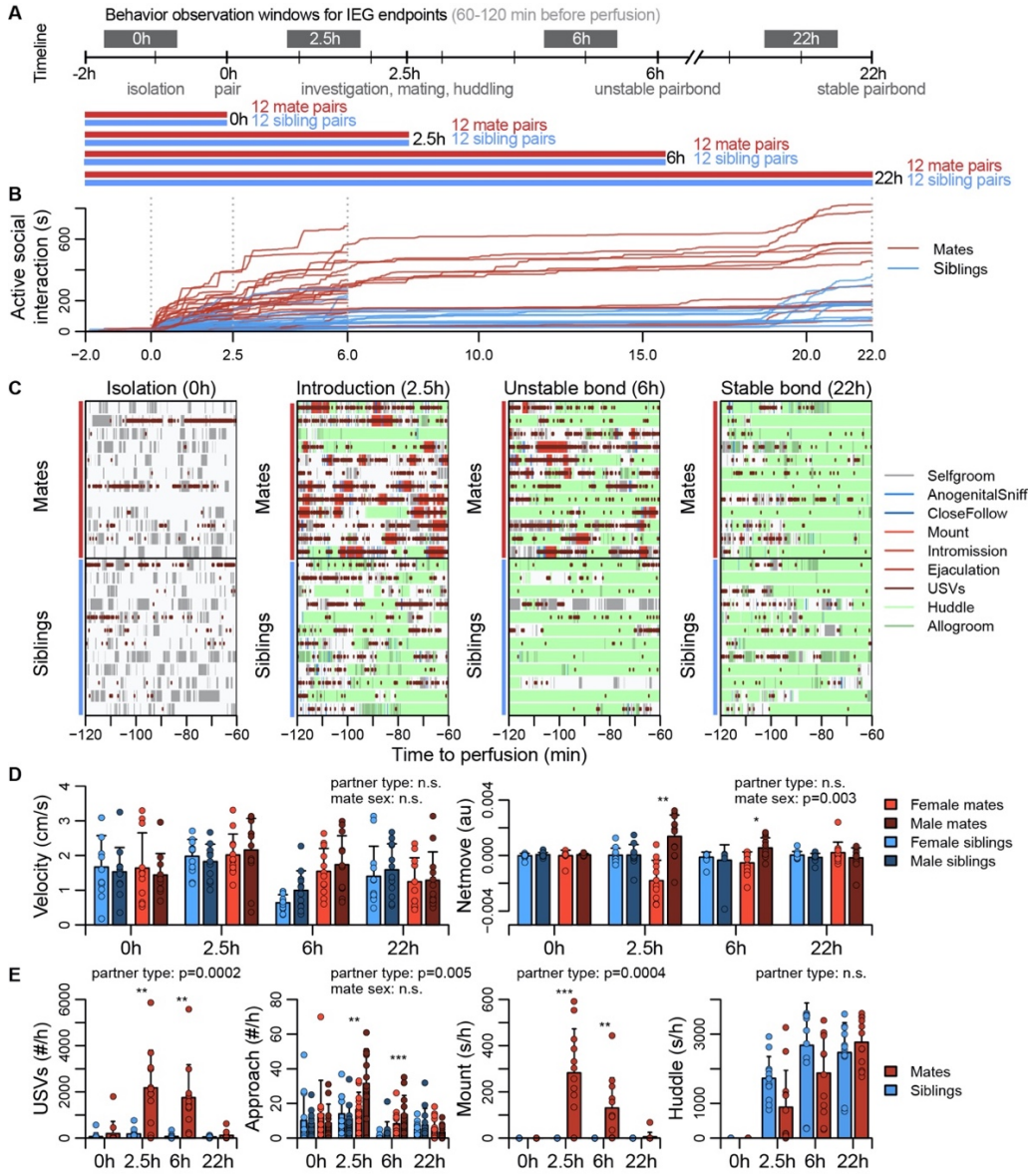

Figure 2. Study design and development of the prairie vole pair-bond. (A) Schematic of the experiment design, where social behaviors (during 1h observations, black blocks) and IEG expression patterns are compared between mate pairs and siblings across time. **(B)** Continuous automated tracking of active social interactions (i.e., an index of social investigation and mating) for mate pairs (red lines) and sibling pairs (blue lines). **(C)** Time courses of specific social behaviors during 1h observation windows for IEG expression, with each row representing one pair. Social behaviors are overlaid onto self-grooming, and ultrasonic vocalizations (USVs, short red ticks) are overlaid onto all behaviors. **(D)** Plots showing group differences (mean ± sd) in individual activity level (velocity) and movement relative to the partner (net move, positive values indicate movement towards the partner). **(E)** Group differences (mean ± sd) in vocal behavior, proximity seeking, mating, and side-by-side contact. For (D) and (E) mate pairs are in red and sibling pairs in blue. Females are a lighter hue and males a darker hue for behaviors measured on an individual (rather than dyadic) level. T-tests were used to compare mates and siblings, and paired t-tests were used to compared female and male mates.

A brain-wide functional neural network for pair-bonding reveals 7 major neuroanatomical clusters, with special prominence for regions of the BST and hypothalamus

Next we measured brain-wide c-Fos immunostaining, a common proxy for neuronal activity and plasticity (Sheng & Greenberg, 1990). To identify brain areas that differed between mate-paired and sibling controls, we used a generalized linear model (GLM) to compare two alternative models. A null model included terms for sex, time, and block; a full model included these variables, as well as pairing status and two interaction terms (pairing*sex, pairing*time). Brain-wide comparisons using voxels or regions of interest (ROI) were largely concordant (Figure 3A-B, Figure Supplement 1b-c, and Video 2), revealing an extensive but specific network of brain regions active during mating and bonding. The brain atlas is organized hierarchically, and of 99 ROIs that differed significantly (permutation test, FDR-corrected $\alpha < 0.1$; Figure 3B), 68 regions were anatomically distinct.

A hierarchical cluster analysis assigned these 68 ROIs into 8 groups (Figure 3C-D, Figure Supplement 1d-e). Each of these groups, or 'clusters,' included multiple brain regions but often centered on a specific structure or group of structures. The purple "BST" cluster, for example, contained regions of the preoptic area and periventricular nucleus of the hypothalamus, as well as multiple substructures within the bed nucleus of the stria terminalis. The blue "POA-VMH" and light blue "PVH" clusters contained multiple regions within the hypothalamus, including the paraventricular nucleus of the hypothalamus, as well as regions of the preoptic area. The green "PFC" cluster was composed of regions within both the prefrontal cortex and olfactory areas. The orange "Amyg" cluster contained the lateral hypothalamus and various olfactory related regions, but the majority of the cluster consisted of amygdalar nuclei such as cortical and medial amygdala and the anterior amygdala area. The light orange "AUD" cluster contained some regions within auditory cortex, and the red "Thal" cluster involved a variety of thalamic regions. The light purple "AOB" cluster contained minimally correlated regions such as the accessory olfactory bulb, and so we do not consider this group to be one of the major clusters. Comparing the groups with connectivity reported in the ARA mouse 'connectome' (Knox et al., 2019) suggests that the 7 major clusters in our dataset are anatomically connected (permutation p=0.0001, Figure Supplement 1f-g).

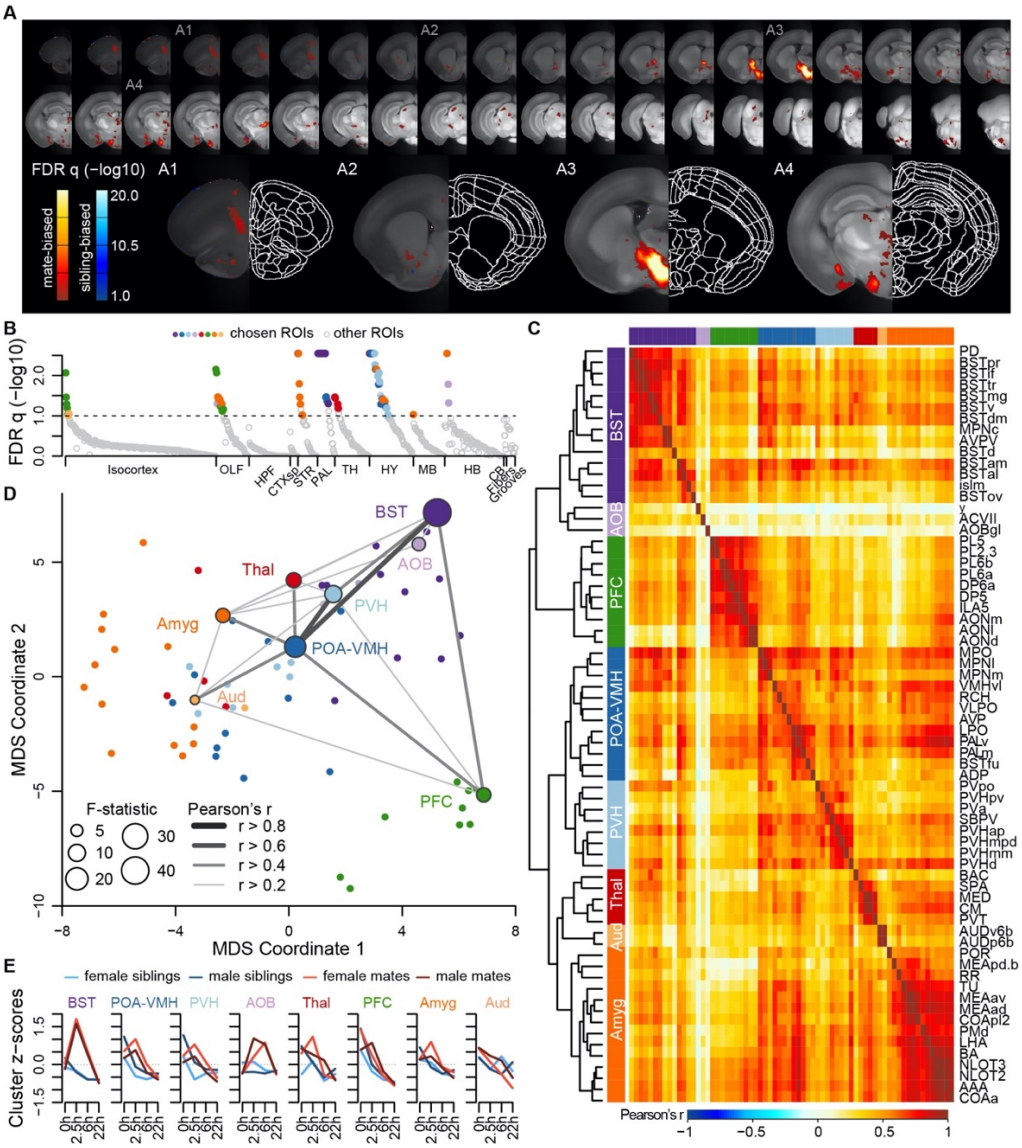

Figure 3. A brain-wide functional network is active during pair-bond formation. (A) Map of bonding-associated voxels. Brightness indicates significance level of comparisons of hypothesized and null models (GLMs) to predict c-Fos cell counts. **(B)** Identification of significant and mutually exclusive ROIs, sorted by anatomical division and F-statistic. The significance levels of these models were determined with a permutation test, by comparing the observed F-statistic to a null distribution of F-statistics from shuffled data (n=10,000 permutations). Colored symbols for ROIs match their cluster group assignments in 3C and 3D. **(C)** Hierarchical clustering of chosen ROIs (n=68) and pairwise Pearson correlations of c-Fos cell counts. **(D)** Multi-dimensional scaling (MDS) coordinate space of the correlations between chosen ROIs. The most significant ROIs per cluster are labelled and their symbol size scaled by the F-statistic. Darkness and thickness of connecting lines reflect correlation coefficients. **(E)** Time course trajectories of total c-Fos cell counts within each cluster. Counts per cluster are scaled across samples and averages taken for each experiment group, with red lines for mates and blue for siblings (females-lighter, males-darker). Each cluster is given labels to summarize the most significant ROIs within them.

Although the nucleus accumbens did not survive multiple test corrections in our ROI analysis (q=0.17), it was significant in univariate analysis (p=0.03), particularly when focused on the 2.5 and 6h timepoints (two sample t-test: t=2.53, p=0.01, Video 2). Furthermore, voxel-level comparisons revealed significant sites within the ventral striatum and the posterior nucleus accumbens (Figure 2A, Figure Supplement 1b-c, Video 2).

Major dimensions of neural and behavioral variation are coordinated among mated pairs

Canonical correlation analysis (CCA) reveals the latent correlational structure within two sets of variables, and so is well suited to compare the principal dimensions of behavioral variation to its neural counterparts (Figure 4, Figure S2f-h). We found that the first canonical correlate (CC1), which defines the largest axis of shared variation in brain and behavior, loaded highly on the BST, POA-VMH, and PVH clusters, as well as on mating-related behaviors (Figure 4A-D). CC1 scores captured responses to mating and bonding in the 2.5h and 6h timepoints (Figure 4A-B). The second canonical correlate (CC2) captured differences between animals who were isolated or paired and loaded particularly highly on the limbic cortical cluster (PFC); we interpret this dimension as capturing appetitive aspects of behaviors (Figure S2f-h).

The first two CC dimensions showed no evidence of sexual dimorphism, while the third dimension suggested subtle but non-significant differences between male and female mates (Figure S2f-g). A formal two-model comparison isolating the effect of the sex*pairing interaction revealed no ROIs that differed following FDR correction. If we limit the comparison to just those 68 areas identified as responding to pairing, we find 29 unique ROIs that exhibit evidence of sex*pairing interaction, although these effects are much weaker than those identified in our above analysis of pairing (Video 2).

Although differences between males and females were modest, the CCA suggested substantial individual differences among mated pairs. We used these data to test whether pairing involved a coordinated change in activities across brain regions. We find that during mating and bond formation (2.5-6h), activity is strongly correlated across ROIs (Figure 4E-F and Figure

250 S2i). Similar to these patterns distributed across putative pair-bonding regions, CC1 brain scores
251 show a strong correlation between male and female mates ($r=0.93$, $p<0.0001$, Figure 4G).

252 Following bonding (22h), within-pair correlations are confined to the coupling of activity
253 between the hypothalamus and amygdala, including between MPOA and medial amygdala. In
254 siblings, who were housed together since birth, hypothalamus-amygdala correlations are
255 relatively uniform across time points, while correlations outside of these regions are largely
256 absent (Figure S2i).

257 The principal nucleus of the BST (prBST), a subregion of the posterior BST, loads highly
258 on CC1 (Figure 4B), and exhibits a strong response to mating in the 2.5 and 6h time points
259 (permutation test, $q=0.003$, Figure 4C); we found that this brain region also shows strong
260 correlations in heterosexual pairs ($r=0.851$, $p<0.0001$, Figure 4G). Remarkably, the number of
261 observed male ejaculations is strongly predictive of prBST c-Fos+ cells in both males and
262 females (males: $r=0.894$, $p<0.0001$; females: $r=0.847$, $p<0.0001$; Figure 4E). To our surprise, but
263 consistent with the canonical correlation analysis, male ejaculation rates were the strongest
264 predictor of activity across brain regions of both sexes (Figure 4D). Statistically controlling for
265 the number of ejaculations effectively abolished the correlation we observed in mated pairs
266 (Figure 4F).

267

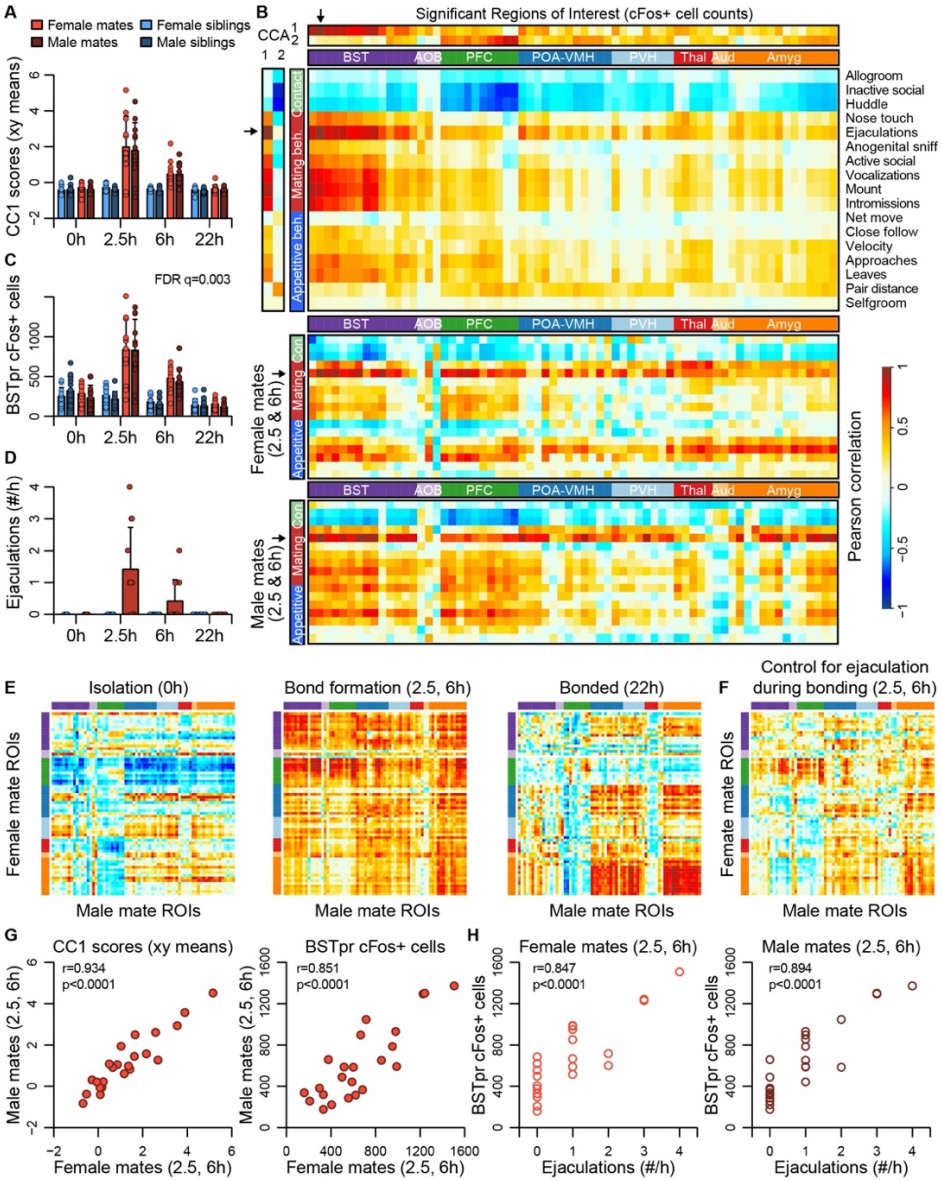

Figure 4. BST emerges as a central hub in the bonding network that is associated with mating success in both sexes. (A) The first dimension of canonical correlation (CC) scores is compared across experiment group (mean ± sd). **(B)** Heatmaps represent correlation coefficients among CC scores, ROI c-Fos cell counts, and behavior measures. The full dataset is on top, and the bottom two correlograms are for female and male mates. For (B), (E) and (F), warm and cool colors represent positive and negative coefficients, respectively. Arrows mark the ROI (BSTpr) and behavior (ejaculation rate) with the strongest correlations to CC1. **(C)** BSTpr activation is compared across groups with a model comparison followed by a permutation test. **(D)** Successful mating events are shown across timepoints (mean ± sd). **(E)** Similarity (i.e., correlation) of bonding network activation is shown in female-male pairs. **(F)** Similarity in bonding network activation is shown in female-male pairs, using partial Pearson correlations to control for ejaculation rate. **(G)** Female-male pair similarity is shown for CC1 scores and BSTpr activation during bond formation. **(H)** Mating success is associated with BSTpr activation for both sexes during bond formation. Pearson correlations were used to assess these associations.

Discussion

Here, we present a brain-wide network of IEG+ circuits active as mating experience elicits a pairbond. We find no evidence of anatomical sexual dimorphism, and only modest evidence of dimorphic function. Our whole-brain mapping of pair-bond formation implicates 68 unique brain regions, including 18 regions that are within the primary brain network proposed for prairie-vole bond formation (Walum & Young, 2018). The 68 identified regions are more strongly anatomically connected to one another than predicted by chance, and so can be interpreted as circuits active during pairing.

Although the majority of regions identified have not been linked directly to bonding, many are logical components of a pair-bonding network. For example, the strongest effects of pairing were detected within a cluster containing multiple compartments of the posterior bed nucleus of the stria terminalis (BST), as well as the posterodorsal preoptic nucleus (PD), core medial preoptic nucleus (MPNc) and anteroventral periventricular nucleus (AVPV; "BST" purple cluster, Figure 3C-E and Figure 4A-C). While this cluster exhibited the strongest response to pairing, only the BST has been previously implicated in prairie-vole bonding (Cushing & Wynne-Edwards, 2006; Lei et al., 2010). The cluster as a whole, however, precisely matches the neural circuitry of male ejaculation previously mapped in rats, gerbils and hamsters (Coolen, 2005; Pfaus, 2009). The posterior BST projects to both the medial preoptic nucleus and the paraventricular nucleus, major contributors to two other clusters ("POA-VMH," blue; "PVH," light blue), regions that also exhibit strong responses to pairing (Cushing et al., 2003; Insel & Young, 2001). The paraventricular nucleus of the hypothalamus, moreover, is a major source of the neuropeptides oxytocin and vasopressin, known modulators of pair bonding in the prairie vole (Walum & Young, 2018).

A fourth cluster ("PFC," green) is composed of prelimbic, infralimbic and olfactory cortex; activity in the vole prefrontal cortex is known to be modulated by hypothalamic oxytocin, and to shape bonding through projections to the nucleus accumbens (Amadei et al., 2017; Burkett et al., 2016; Horie et al., 2020). In addition to its effects on the PFC, pairing drove increased c-Fos expression in the ventral pallidum, a major node in reward circuity, as well as in the paraventricular nucleus and the medial preoptic area, modulators of reward. Thus, the absence of widespread c-Fos induction in the nucleus accumbens seemed puzzling (but see

313 (Curtis & Wang, 2003)). However, the accumbens was significant in univariate tests, as well as
314 in voxel-level analyses. Overall this result is consistent with pharmacological,
315 electrophysiological, and calcium-imaging data on the role of the nucleus accumbens in prairie
316 vole bonding (Amadei et al., 2017; Aragona et al., 2006; Scribner et al., 2020). The absence of
317 significant effects at the level of the entire nucleus accumbens together with the presence of
318 anatomically restricted voxel-level significance suggests substantial anatomical heterogeneity in
319 the contributions of the nucleus accumbens to bond formation.

320 Our data suggest that pairing-related cFos immunoreactivity is largely shared across
321 sexes, and that much of the pairing related activity is driven by mating behavior. The strongest
322 signal of pairing status was in the prBST, a region important in male ejaculation (Insel & Young,
323 2001; Pfaus, 2009). We found that both sexes exhibited the strongest signal of pairing status in
324 prBST. This finding supports supports recent work in mice showing that different neural
325 populations in prBST, aromatase+ and Vgat+ neurons, respond to ejaculation in males and
326 females (Bayless et al., 2019). Moreover, we found a surprisingly strong relationship between
327 ejaculation rates and brain-wide activity patterns across the putative pair-bonding circuit. The
328 concordance between males and females was surprising, but is consistent with IEG studies of
329 ejaculation and related circuitry in male and female rats (Coolen, 2005; Pfaus, 2009). These data
330 are also consistent with the interpretation that copulation enables coordination and assessment
331 during bonding (Carter et al., 1995; Dewsbury, 1988; Eberhard, 1996; Getz et al., 1993).

332 The tight coupling of widespread neural activity adds to the growing number of examples
333 – including fish, mice, bats, and humans – that demonstrate correlated neural function across
334 socially interacting individuals (Hasson et al., 2012; Kingsbury et al., 2019; Kinreich et al., 2017;
335 Long et al., 2020; Vu et al., 2020; Zhang & Yartsev, 2019). Although widespread differences
336 among mated pairs seem to be driven by ejaculation rates during mating and bonding, a smaller
337 subset of circuits – specifically connections between the hypothalamus and amygdala – remain
338 correlated after pairing. The similarity of this post-pairing pattern to non-sexual affiliative
339 mechanisms recently documented in lab mice (Hu et al., 2021), and to correlations we observe
340 among sibling pairs, suggests these regions play a role in both reproductive and non-reproductive
341 attachment.

342

343 *Ideas and Speculation*

344 This brain-wide map of IEG induction provides a uniquely comprehensive perspective on the
345 circuits that enable sexual behavior to become a bond. To help organize this enormous dataset,
346 we looked to existing literature to compare the implicated circuits to those related to sociosexual
347 behaviors in other species (Figure 5A, B). Overlaying the time course of behaviors and circuit
348 activity suggest distinct stages of bonding and attendant neural function. We divide those stages
349 into mating, bonding, and ongoing bond maintenance.

350 The first canonical correlate captured the major dimensions of both brain and behavioral
351 variation, and showed the largest group differences surrounding the 2.5 hr timepoint.
352 Behaviorally, this difference mapped strongly onto mating behavior, and in particular to rates of
353 male ejaculation. The neural circuits of rodent sexual behavior in general, and of male
354 ejaculation in particular, have been well studied in rats, hamsters and laboratory mice (Bayless et
355 al., 2019; Pfaus & Heeb, 1997; Veening et al., 2014; Veening & Coolen, 2014). In this context,
356 chemosensory signals are thought to drive activity in MeA, MPO, and PVH. Copulation drives
357 activity in MPN, PD, VMH and BST. We found that elevated cFos induction levels occur in
358 these areas early on in the bonding timecourse and then decline. Such findings support the idea
359 that these core circuits orchestrate early social interactions that enable individuals to process
360 chemosensory signals and then initiate lordosis, mounting, and ejaculation. Our study also
361 revealed a set of regions that have yet to be emphasized in socio-sexual circuits, including lateral
362 hypothalamic area and lateral preoptic area. While research on these regions emphasize non-
363 social functions, a number of studies suggest that these regions play a role in social behaviors, or
364 participate in goal-directed behavior and reward (Chen et al., 2021; Nieh et al., 2016; Petzold et
365 al., 2023).

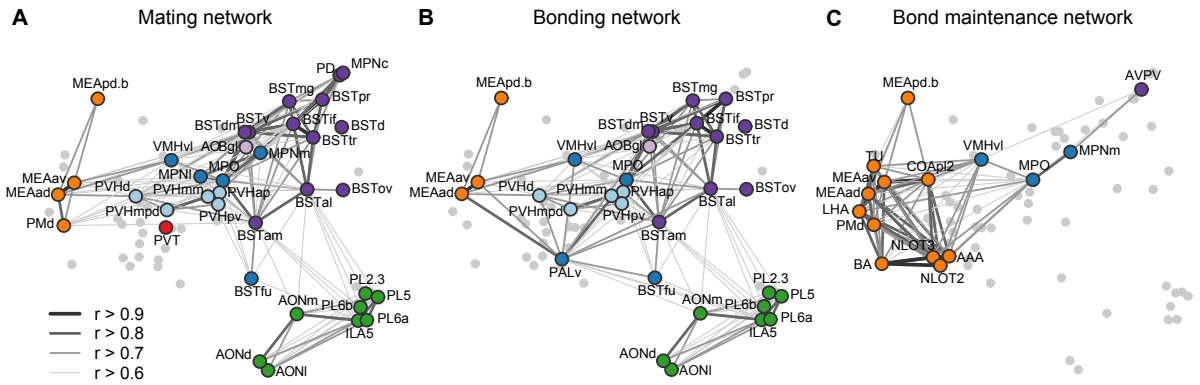

Figure 5. Working model for neural systems that shape stages of pair-bond development. **(A)** Schematic of the network of regions identified in our study overlaid with regions known to be involved in rodent mating behavior (Pfaus & Heeb, 1997; Veening et al., 2014; Veening & Coolen, 2014). This network is proposed to be involved during the early stages of bond formation (e.g., 2.5 h timepoint). **(B)** Schematic of the network of regions identified in our study overlaid with regions known to be involved in prairie vole pair-bonding behavior (Walum & Young, 2018; K. A. Young et al., 2011). This network is proposed to be involved with the middle stages of bond formation when animals are engaged in prolonged mating and affiliative interactions (e.g., 6 h timepoint). **(C)** Schematic of the network of regions that are correlated between female and male mates at the 22 h timepoint in this study. These are identified from pairs of regions in which both sexes show high inter-individual similarity (Pearson correlation, r > 0.75). This network is proposed to be involved with the recognition and convergence of behavioral state in bonding partners. The network schematics in (A), (B) and (C) are adapted from the multi-dimensional scaling of correlations between region activity (Figure 3D). Light gray points represent regions not included in the proposed network. Line thickness and darkness between colored regions represent Pearson correlation r values between the connected regions.

Interestingly, one anomaly from the literature on sexual behavior circuits is that females also show IEG induction associated with male ejaculation – a finding evident in both rats and mice (Pfaus & Heeb, 1997; Veening et al., 2014). Similarly, recent work in female laboratory mice demonstrate that Vgat+ neurons in the prBST exhibit responses to male ejaculation (Bayless et al., 2019). The extraordinary pattern of coordination we observe between members of a pair across nearly 70 brain regions, and its prediction by male ejaculation, suggest that both males and females are experiencing similar and profound affective states. Moreover, the fact that repeated copulation is necessary for bonding is consistent with work in a variety of taxa suggesting that repeated copulation is a means of partner assessment (Dewsbury, 1988; Eberhard, 1996); in prairie voles, we suggest that both males and females are assessing the ability of a male to monopolize a female, a trait that would predict male paternity and ability to

395 defend a nest against conspecifics in the field. Pfaus and others have argued that females of other
396 species, including laboratory rodents, exhibit orgasm-like responses (Georgiadis et al., 2012).
397 Although our current data are unable to address this claim directly, the hypothesis offers a
398 parsimonious interpretation of our data, and the topic merits further scrutiny.

399 In this circuitry, the "extended amygdala" regions of the BST and MeA stand out for their
400 extensive projections to and from the hypothalamus, and for their known roles in individual
401 recognition. Dumais et al (2016), for example, have documented that the BST of the rat is
402 essential to individual recognition; in parallel, Knoedler et al (2022) find that ERa in the BST
403 coordinates sex recognition in laboratory mice. Most directly, Cushing and colleagues have
404 shown that ERa in the BST is essential to the formation of pairbonds in prairie voles (Lei et al.,
405 2010). Similarly, oxytocin actions in the MeA are known to govern social recognition in lab
406 mice (Ferguson et al., 2001). We hypothesize that IEG induction in response to mating enables
407 the identity of a mate to get access to the modulation of hormonal and behavioral states by the
408 hypothalamus. Such identity representations may coordinate partner-specific patterns of
409 neuropeptide release (PVN), selective aggression (VMHvl), selective mating (VMHvl, MPOA),
410 and social reward (MPOA).

411 After bond formation and stabilization, we find that that mated pairs are similar to co-
412 housed siblings in terms of brain-wide IEG induction patterns (Figure 5C). More remarkable, is
413 that after 22 hrs both co-housed siblings and mated pairs show strong correlations in amygdala
414 IEG induction, particularly in the MeApd. We propose that this correlated activity reflects a
415 sensitivity to the behavioral state of a partner that emerges as a function of bonding. Recent work
416 has revealed that in laboratory mice, tachykinin+ GABAergic neurons project from the MeApd
417 to the MPOA, where they contribute to both consolation grooming and social reward (Hu et al.,
418 2021; Wu et al., 2021). These projections have not been implicated in pairbonding, but our
419 current data suggest this circuit may play a broader role in the ongoing function of the
420 relationships of both mates and siblings. Since prairie voles often live in larger family groups
421 (Getz et al., 1993), particularly over winter, a common mechanism for the maintenance of
422 familial and sexual bonds would be consistent with their ecology. In addition, the strong
423 correlation of activity across a variety of related amygdala and associated regions suggest this
424 circuit may be much broader than the interactions between MeApd and MPOA documented in
425 laboratory mice.

Conclusions

Overall, our data survey the brain to identify circuits active as mating produces a pairbond. These data allowed strong tests of opposing hypotheses about sexual dimorphism and coordination during bonding (de Vries, 2004; Hasson et al., 2012; Kingsbury et al., 2019; Kinreich et al., 2017; Long et al., 2020; Zhang & Yartsev, 2019), revealing a surprising absence of sexual dimorphism in structure and function, and an extensive coordination of neural activity among new pairs. We confirm the activity of known regulators of mating and bonding such as reward circuits, the paraventricular nucleus and the bed nucleus of the stria terminalis (Coolen, 2005; Insel & Young, 2001; Lei et al., 2010; Pfaus, 2009); we map a path by which sexual activity finds its way to known regulators of bonding, and identify a variety of novel regions and circuits whose roles in bonding remain to be examined. Our results suggest a novel model in which the BST is a key node connecting sexual experience to the neuroendocrine functions of the hypothalamus and preoptic area, and that coupling between the preoptic area and the amygdala may play an unappreciated role in the maintenance of an established bond. Manipulations of these circuits and their behavioral consequences offer rich new opportunities for research into the mechanisms of bonding and their contributions to well-being.

445 **Materials and Methods**

446

447 *Animals*

448 Prairie voles (*Microtus ochrogaster*) used in behavioral and anatomical experiments were prairie
449 voles derived from wild-caught voles from Jackson County, Illinois and bred at The University
450 of Texas at Austin. At weaning (PND 21), voles were housed in polycarbonate cages (R20 Rat
451 Cage, Ancare Corp., NY) in groups of 2-5 same-sex littermates and provided with standard
452 rodent chow (LabDiet 5001, Lab Supply, TX) and water *ad libitum*. Temperature of the colony
453 room was maintained at a controlled temperature (20-23°C), and the photoperiod was on a 12:12
454 light:dark cycle (lights on: 0600, lights off: 1800). Housing arrangements allowed animals to
455 receive visual and olfactory cues, but not tactile contact, with conspecific males and females.
456 Mice used for anatomical research were housed with ad libitum access to food and water in a
457 controlled temperature (21-22°C) and light (12:12 light/dark cycle) room. All animal procedures
458 were approved by the Institutional Animal Care and Use Committees at the University of Texas
459 at Austin and Cold Spring Harbor Laboratory.

460

461 *Brain tissue sample preparation and processing*

462 Prairie voles underwent intracardiac perfusion ~20 min (mean = 21 min, range = 10-40 min)
463 minutes after the behavioral observation endpoints (2h acclimation or 2h acclimation in addition
464 to 2.5h, 6h or 22h cohabitation). Animals were anesthetized with open-drop isoflurane exposure,
465 exsanguinated with 0.9% saline (2 min 30 s at 13 mL/min), and fixed with 4% paraformaldehyde
466 (PFA) in 0.05M PB (5 min 30 s at 13 mL/min). All harvested brain tissue samples were post-
467 fixed overnight at 4° C in 4% PFA in PB. After post-fixation, samples were washed 3x in 0.05M
468 PB and stored in 0.05M PB 0.02% sodium azide at 4° C until immunolabeling processing.

469 Mice of 8-10 weeks old were anesthetized with ketamine/xylazine and transcardially
470 perfused with isotonic saline followed by 4% PFA in 0.1M phosphate buffer (PB, pH 7.4).
471 Brains were extracted and post-fixed overnight at 4° C in the same fixative solution, and stored
472 at 0.05M PB until immunolabeling processing.

473

474 *Whole brain IEG staining and imaging*

475 Right hemisphere of all brain samples were cut and immunolabeled for c-Fos and posteriorly
476 cleared using iDisco+ protocol (Renier et al., 2014, 2016). Briefly, samples were initially
477 delipidated with methanol and later permeabilized and blocked with DMSO and donkey serum
478 respectively. Thereafter, all samples were incubated with c-Fos antibody and Alexa Fluorophore
479 647 secondary antibodies. Samples were cleared with increasing concentration steps of methanol
480 and dichloromethane as previously described (Renier et al., 2014, 2016). After clearing, samples
481 were imaged sagittally on a light-sheet fluorescence microscope (Ultramicroscope II, LaVision
482 Biotec). Samples were imaged continuously every 5um at 640 nm and 488 nm, for signal and
483 background channels respectively.

484

485 *Construction of the vole reference brain and atlas*

486 For the construction of the prairie vole reference brain, 190 brains from c-Fos+ cell counting
487 analysis were co-registered as described above (see 3D registration of the vole brain and
488 Anatomical features enhancing registration) (Kim et al., 2015).

489 For the construction of the prairie vole reference atlas, the Allen Reference Atlas (ARA)
490 was initially used as a template. After initial registration, output transformations were used to
491 warp mouse atlas onto the prairie vole reference brain. In order to validate atlas registration,
492 prairie vole Neurotrace stained brains were registered at high resolution onto the prairie vole
493 reference brain.

494

495 *3D registration of the vole brain*

496 Brains were registered to a standardized reference brain as previously described. Initial
497 3D affine transformation was calculated using 6 resolution levels followed by a 3D B-spline
498 transformation with 3 resolution levels. Similarity was computed using Advanced Mattes mutual
499 Information metric by Elastix registration toolbox. In order to enhance image registration, both
500 brain images and reference brains were pre-processed to reduce the impact of imaging artifacts
501 during the computation of mutual information (Video 1). First, brain image illumination was
502 corrected to homogenize illumination across sections. Second, both brain images and reference

503 brain intensities were smoothed to reduce imaging artifacts (Muñoz-Castañeda & Osten;
504 manuscript in preparation) (Muñoz-Castañeda et al., 2021).

505

506 *Whole brain prairie vole Neurotrace staining*

507 Whole brain Neurotrace staining (Figure 1 and Figure Supplement 1a) was performed with a
508 modification of iDISCO+ protocol. Samples were initially washed in phosphate-buffered saline
509 (PBS) and incubated for in PBS + TritonX-100 + DMSO + glycine. Then samples were
510 transferred and incubated in a solution with PBS and Neurotrace. Finally, samples were washed
511 in PBS (Muñoz-Castañeda & Osten, manuscript in preparation) (Muñoz-Castañeda et al., 2021).

512

513 *Comparison of vole and mouse neuroanatomy*

514 For area-based volume quantifications the reference brain was register onto each single imaged
515 brain and all volume areas were automatically quantified with custom made scripts (Muñoz-
516 Castañeda & Osten, manuscript in preparation) (Muñoz-Castañeda et al., 2021).

517

518 *STPT whole brain imaging for anatomical delineation*

519 Before imaging, both prairie vole and mouse brains were embedded and cross-linked with
520 oxidized 4% agarose as previously described (Kim et al., 2017; Ragan et al., 2012). Whole brain
521 imaging was achieved using the automated whole-mount microscopy STPT. The entire brain was
522 coronally imaged at an X,Y resolution of 1µm and Z-spacing of 50µm (Kim et al., 2017; Ragan
523 et al., 2012). After imaging, brains were registered to the reference brain for anatomical
524 validation (see 3D registration of the vole brain).

525

526 *Automated c-Fos+ cell detection*

527 c-Fos+ cells segmentation was performed using convolutional neural networks as previously
528 described (Kim et al., 2016, 2017). After cell segmentation, all cell centroids were calculated for
529 whole brain distribution analysis. For the analysis of area-based c-Fos+ cell counts, the mouse
530 reference brain was registered onto each prairie vole brain, using the output transformations to

531 warp the atlas onto each individual brain for ROI cell counting and distribution. For voxel
532 analysis, the inverse transformation output was used to move all cFos+ centroids onto the
533 reference brain.

534

535 *Experiment design*

536 Study subjects were 8 to 12 week old sexually naïve prairie voles. There were eight treatments
537 that varied based on partner type and cohabitation time (Figure 2). Subjects were partnered with
538 a familiar same-sex cage mate ("siblings") or an opposite-sex individual ("mates") for 0, 2.5, 6,
539 or 22 hours. The 0 h timepoint represents a baseline state before pairing takes place, the 2.5 h
540 time point is ~2 h after the first mating bout, the 6 h time point is when an unstable partner
541 preference is established, and the 22 h time point is when pair-bonding becomes stable (i.e., after
542 overnight mating) (DeVries & Carter, 1999; Williams et al., 1992). The experiment was run in
543 six testing blocks. Each block was composed of eight testing days spread across two weeks, with
544 two adjacent testing days per cohabitation time point (0, 2.5, 6, 22 h). Two pair sets were tested
545 in a day, either male siblings and female siblings or two mating pairs. The order of partner type
546 (adjacent days per time point) and order of cohabitation timepoints (four per block) were
547 counterbalanced across blocks. Individuals were randomly assigned to the partner type condition.

548 There were 12 sibling pairs and 12 mating pairs tested for each cohabitation time point,
549 for a total of 96 female and 96 male study subjects. Of this total, 190 voles were used for
550 behavioral analyses, and 189 voles were used for IEG analyses. A mating pair from the 0 h
551 timepoint group lacked behavioral data due to a camera malfunction (audio was unaffected).
552 Three brain samples were not used in IEG analyses: 1 male sibling from the 6 h timepoint group,
553 1 female mate from the 0 h time point, 1 female mate from the 6 h time point). The first sample
554 was not stained for c-Fos due to major issues with the perfusion. The latter two samples were
555 identified as outliers by a Rosner's test (EnvStats R package (Millard, 2013)); their whole-brain
556 c-Fos counts were higher than the rest of the samples ($R = 4.61$ and 5.504, $P < 0.05$).

557

558 *Behavioral procedures*

559 Voles were housed in new home cages, isolated from their sibling cage mates, 4-5 days prior to
560 testing. During this isolation period, females induced into estrus with daily 0.1 ml subcutaneous
561 injections of 2 μg estradiol benzoate dissolved in sesame oil (Amadei et al., 2017; Carter et al.,
562 1988). Voles were screened for mating capacity on the 3rd day of isolation. This screening
563 involved a brief exposure (< 10 min) to an opposite-sex vole until the first mount. Voles that did
564 not show a mating attempt in the first exposure were retested with a different animal. We used
565 this mating assay to restrict study subjects to voles that showed lordosis and mounting behavior.

566 Behavioral testing began in the morning after lights-on between 8:00 and 10:15 (mean =
567 8:44 am). Subjects were fitted with colored collars (pipe cleaner attached to a miniature cable tie)
568 for identification and automated video tracking. Then, subjects were placed on opposite sides of
569 a custom made acrylic testing arena (12" x 24" x 12"), separated by an opaque divider, for a 2 h
570 acclimation period. The testing arenas were outfitted with fresh bedding and ad libitum access to
571 chow and water and were housed within an enclosed experiment box (42" x 34" x 24")
572 constructed from expanded PVC. These experiment boxes had controlled white:red lighting
573 (Phillips Hue light strips) on the same photoperiod cycle as the colony room. For the 0 h time
574 point subjects only underwent the acclimation period. Otherwise, the divider was removed at the
575 end of acclimation so that subjects could interact freely for 2.5, 6 or 22 h. After this acclimation
576 (0 h group) or cohabitation (2.5, 6, 22 h groups), subjects were promptly removed from the arena
577 and perfused. Arenas were cleaned with 70% EtOH between tests.

578 Video and audio data were recorded from Basler Ace-IMX174 cameras (1920x1200, 2
579 MP resolution, Basler AG, PA) and Ultramic 364K BLE microphones (Dodotronic, Italy)
580 suspended above each testing arena. Cameras were outfitted with a 16 mm lens and 46mm linear
581 polarizer. Video data were recorded with Pylon viewer (v 5.1.0.12681, Basler AG, PA) at 25 fps
582 with white balance set to ~1.93 and exposure levels between 15 and 25 ms. Audio was recorded
583 with SeaPro2 software (v 2.0j, CIBRA) at a 192 kHz sampling rate and saved in 30 min WAV
584 files (starting on the hour and every half hour). With this set up, ultrasonic vocalizations (USVs)
585 could be detected per pair, but not localized to specific individuals. Recording equipment was
586 connected directly to a Windows 10 PC. The start of both video and audio recordings were
587 timestamped with PC system time, which enabled the synchronization of video-audio data on a
588 second-by-second timescale.

589

590 *Video and audio processing*

591 Behaviors were measured during observation windows that corresponded to peaks in IEG
592 expression (Kim et al., 2015; Renier et al., 2016), specifically 60-120 min before each pair's
593 perfusion (i.e., midpoint between exsanguination times of each vole pair). Both automated and
594 manual methods were used to characterize vole behavior.

595 Automated scoring of movement and proximity behaviors was done with Ethovision (v
596 10.1). Individual collars were tracked during white light periods, with detection settings set for
597 each video and optimized for collar color (blue / green, mean ± sd: huemin = 97.0 ± 1.4 / 63.1 ±
598 2.5, huemax = 113.0 ± 1.4 / 79.2 ± 2.6, saturationmin = 113.3 ± 11.8 / 85.4 ± 10.5, saturationmax
599 = 255.0 ± 0.2 / 254.9 ± 0.7, brightnessmin = 84.1 ± 10.5 / 70.2 ± 8.9, brightnessmax = 254.0 ±
600 4.6 / 254.7 ± 1.6, marker size = 50). Body area was recorded across both white light and red light
601 periods with the grayscaling method (white / red light: detectionmin = 0, detectionmax = 108.7 ±
602 3.3 / 5.96 ± 0.8, pixel sizemin = 3,000, pixel sizemax = 125,000, contour erosion = 1, contour
603 dilation = 1). The largest body area was recorded when animals were separated. Overall activity
604 (% pixel change between frames) also was recorded for white light and red light periods
605 separately (white / red light: threshold = 1, background = 10, compression = "on" for all 24
606 overnight videos / "on" for 18 overnight videos). Individual tracking, body area, and activity
607 were recorded at 12.5 samples/s, down sampled to 1/s, and used to compute an array of
608 behavioral measures across entire recording sessions and the 1 h IEG induction windows (Figure
609 S2a-d and Supplemental File 3).

610 Manual scoring of mating, investigative, grooming, and contact behaviors was done with
611 BORIS (v 7.9.6) (Friard & Gamba, 2016). Two trained observers, who were blind to study
612 animals' sex and partner condition, independently labelled social and non-social behaviors in
613 cohabitation videos (2.5, 6, 22 h groups) during the 1 h IEG induction windows (Supplemental
614 File 3). Self-grooming during in isolation videos (0 h group) was labelled by one of the trained
615 observers. Inter-observer reliability was assessed with Pearson correlations. For dyadic behaviors
616 (e.g., mounting, huddling), reliability was assessed across vole pairs. For individual behaviors
617 (e.g., anogenital sniffing, self-grooming), reliability was assessed separately for individuals with

618 blue collars and green collars. All behaviors had high agreement between independent observers
619 (Pearson correlations, r > 0.85, Supplemental File 3).

620 Ultrasonic vocalizations (USVs) were detected with DeepSqueak (v 2.6.1 in MATLAB
621 2019a) (Coffey et al., 2019). To initially label USVs, the "AllShortCalls" network was used
622 along with the following detection settings: frequency range of 20-90 kHz, overlap of 0.1s, 5s
623 chunk length, and a high precision recall. Then, a trained observer revisited all USVs labels
624 during the 1h behavior observation windows. Using the DeepSqueak interface, the observer
625 removed labels of background noise (e.g., water bottle sounds) and adjusted USV label
626 boundaries to exclude noise. This trained observer was blind to the experiment condition
627 (siblings vs mates), caller sex, and the behavioral context. The start and stop times of all USV
628 labels were exported and the times were adjusted to align with the video frame timestamps.

629

630 *Statistical analyses*

631 Absolute and relative volumes of brain regions were compared across species (mouse vs. vole)
632 and sexes (male voles vs. female voles) with negative binomial regression models (Supplemental
633 Files 1 and 2). Relative volumes were computed as the ratio of region volumes to whole brain
634 volumes. To control for false discovery rate, p-values were corrected for multiple comparisons to
635 q values (Hochberg, 2015).

636 All statistical analyses for behavioral experiments were carried out in R (v 3.5.3) (R
637 Development Core Team, 2016). Welch two-sample t-tests were used to compare behavioral
638 measures between mate pairs and sibling controls. Paired t-tests were used to compare behavioral
639 measures between female mates and male mates. T-tests were run for all timepoints combined
640 and for specific timepoints. Significance values were adjusted for multiple comparisons using the
641 FDR method, with an alpha threshold of q=0.05. Pearson correlations were used to make
642 associations between behavioral measures and ROI c-Fos+ cell counts (Figure S2e,h,i).

643 To identify brain regions that are sensitive to pairing status, we used a model comparison
644 approach. For each voxel or ROI, two general linear regression models (with a quasi-poisson link
645 function to model over-dispersed count data) were used to predict IEG c-Fos expression across
646 all individuals (n=189) (Figure 3, Video 2). These models differed in whether the partner

condition (sibling vs. mate) was a part of the formula. The "null" model (Equation 1) included main effects of sex [S], time point [T], and experiment block [B]. The hypothesized "bonding" model (Equation 2) included the same predictor terms in addition to a main effect of partner type [P] and interactions between partner with sex or timepoint. In these models, sex was a categorical factor (males vs females). Time point was an ordinal variable from 1 to 4 (0, 2.5, 6, 22h) and was included as a polynomial term to account for both linear and quadratic (i.e., 0/22h vs 2.5/6h) effects. Block was an ordinal variable from 1 to 6. Partner was a categorical variable (mates vs siblings). This model comparison allowed for the identification of voxels/ROIs where c-Fos expression variation was better explained better when accounting for the partner condition.

(Equation 1) $Y_i = \beta_1 S_i + \beta_2 T_i + \beta_3 T_i^2 + \beta_4 B_i + e_i$

(Equation 2) $Y_i = \beta_1 S_i + \beta_2 Ti + \beta_3 T_i^2 + \beta_4 B_i + \beta_5 P_i + \beta_6 P_i{*}S_i + \beta_7 P_i{*}T_i + \beta_8 P_i{*}T_i^2 + e_i$

The null and bonding GLMs were compared with an ANOVA test. For the ROI-level analysis, a Monte Carlo approach (10,000 random shuffles of the data) was used to determine a null distribution for the ANOVA F-statistics and compute p-values. For the voxel- and ROI-level analyses, the FDR method was used to correct for multiple tests, with an alpha threshold of q=0.1.

We ran an additional model comparison to specifically test for sex differences in c-Fos expression (Video 2). In this analysis, we compared the full version of the model formula (Equation 2) to a reduced version of the model (Equation 3). The reduced model excludes a sex by partner interaction term. The FDR method was used again to correct for multiple tests across all voxels and all ROIs, with an alpha threshold of q=0.1.

(Equation 3) $Y_i = \beta_1 S_i + \beta_2 T_i + \beta_3 T_i^2 + \beta_4 B_i + \beta_5 P_i + \beta_6 P_i{*}T_i + \beta_7 P_i{*}T_i^2 + e_i$

ROIs were chosen for subsequent analyses if they were significant in the Equation 1 vs. Equation 2 model comparison and were mutually exclusive with one another. To select mutually exclusive ROIs, we constructed an structural hierarchy from the ARA. For any significant ROIs that overlapped anatomically, we iteratively chose the ROI with the higher ANOVA F-statistic. This method excluded larger brain regions in lieu of smaller and more localized ROIs.

674 Significant "chosen" ROIs were assigned to groups by using hierarchical clustering with the
675 ward D2 method with a Euclidean distance matrix extracted from c-Fos cell counts (Murtagh &
676 Legendre, 2014; R Development Core Team, 2016). The resulting tree was cut at such that ROIs
677 were grouped into anatomically similar clusters (Figure 3, Figure Supplement 1f,g). We used
678 multi-dimensional scaling (MDS) to further interpret the degree of similarity between chosen
679 ROIs and their clustering groups based on the Euclidean distance matrix (Figure Supplement 1e).
680 The MDS method is a form of non-linear dimensionality reduction to visualize similarity in
681 Cartesian space (Cox & Cox, 2008).

682 To confirm whether chosen ROI clusters represented structural circuits, we compared
683 cluster assignments to published data on structural connectivity in the mouse brain (Knox et al.,
684 2019) (Figure Supplement 1f,g). First, we refined a matrix of ROI-ROI ipsilateral normalized
685 connection densities to align with our list of chosen ROIs. Some of our chosen ROIs did not
686 align with this matrix because they represented subregions of the ROIs in the matrix. In those
687 cases, we used data from the next inclusive ROI that was available (e.g., BST data used for
688 BSTpr). Then, for each cluster, we found the mean normalized connection density between the
689 regions. We excluded data from the matrix diagonals (e.g., BST to BST) to emphasize
690 connections between, rather than within, regions. We took an average of these cluster densities
691 values to capture the overall connection density based on our cluster assignments. A permutation
692 test was used to assess whether this connection density was higher than expected by chance. The
693 rows of the connectivity matrix (rows = origin ROIs, columns = target ROIs) were randomly
694 shuffled prior to computing the average cluster density, and this was done 10,000 times to
695 construct a null distribution. This null distribution was then compared to the observed density to
696 estimate its probability.

697 We used canonical-correlation analysis (CCA) was used to investigate the relationships
698 between behavioral variables and IEG induction patterns in chosen ROIs. CCA is an
699 unsupervised method that finds linear combinations of two variable sets with the strongest
700 correlation (González et al., 2008; R Development Core Team, 2016; Wang et al., 2020). This
701 approach enabled us to isolate discrete canonical correlates (CC), where each individual animal
702 is assigned scores for each variable set per CC factor (Figure S2i). We used correlations between
703 individual behavior/ROI measures and their CC scores to interpret CC factors and identify

704 specific behaviors and ROIs with the strongest associations. Wilk's lambda test statistic was used
705 to confirm which CC factors represented a significant association between the two variable sets.

706

707 **Data and Code availability**

708 Source data and code will be made publicly available on Figshare upon acceptance of the
709 manuscript (Files can be accessed here prior to publication:
710 https://figshare.com/s/c64462fef32b3b43e452). The prairie vole reference brain and annotation
711 atlases will be made accessible through GitHub (https://github.com/rodrigomc84/PrairieVole-
712 Atlas.git). Raw behavioral and neural data will be made available upon reasonable request.

713

714 **Acknowledgments**

715 We thank animal resource staff at the University of Texas at Austin and Cold Spring Harbor
716 Laboratory for their assistance with animal care and husbandry. T. Burkhard helped with animal
717 perfusions and tissue collection, and D. Lama and M. Klein assisted with behavior scoring. We
718 thank J. Collins and other staff at Certerra Inc. for their assistance with immunohistochemistry,
719 whole-brain imaging and preliminary analyses, and we thank K. Pradhan for advice on
720 customizing the voxel and ROI analysis pipeline. R. Drewes and J. Palmer assisted with
721 alignment of the reference atlas to the prairie vole brain and with imaging. J. Tollkuhn provided
722 additional prairie voles for species comparisons and immunohistochemistry. Finally, we thank
723 Drs. H. Hofmann. A. Kepecs, M. Long, and M. Ryan for their feedback on earlier versions of
724 this manuscript. This research was funded by grants from the National Institutes of Health:
725 R01MH115267 (S.M.P., P.O.) and K99MH126164 (M.L.G.).

726

727 **Author contributions**

728 All authors conceptualized the research. M.L.G. and R.M.C. performed the research and
729 analyses. S.M.P. and P.O. supervised the research. M.L.G. and S.M.P. wrote the paper. All
730 authors reviewed and edited the paper.

731

Competing interests

P.O. is a co-founder, shareholder and Director at Certerra, Inc and co-founder, shareholder and President at Certego Therapeutics, Inc. All other authors declare no competing interests.

References

Amadei, E. A., Johnson, Z. v., Jun Kwon, Y., Shpiner, A. C., Saravanan, V., Mays, W. D., Ryan, S. J., Walum, H., Rainnie, D. G., Young, L. J., & Liu, R. C. (2017). Dynamic corticostriatal activity biases social bonding in monogamous female prairie voles. *Nature*, *546*(7657), 297–301. https://doi.org/10.1038/nature22381

Aragona, B. J., Liu, Y., Yu, Y. J., Curtis, J. T., Detwiler, J. M., Insel, T. R., & Wang, Z. (2006). Nucleus accumbens dopamine differentially mediates the formation and maintenance of monogamous pair bonds. *Nature Neuroscience*, *9*(1), 133–139. https://doi.org/10.1038/nn1613

Baumeister, R. F., & Leary, M. L. (1995). The need to belong: Desire for interpersonal attachments as a fundamental human motivation. *Psychological Bulletin*, *117*(3), 497–529.

Bayless, D. W., Yang, T., Mason, M. M., Susanto, A. A. T., Lobdell, A., & Shah, N. M. (2019). Limbic neurons shape sex recognition and social behavior in sexually naive males. *Cell*, *176*, 1190–1205. https://doi.org/10.1016/j.cell.2018.12.041

Bendesky, A., Kwon, Y. M., Lassance, J. M., Lewarch, C. L., Yao, S., Peterson, B. K., He, M. X., Dulac, C., & Hoekstra, H. E. (2017). The genetic basis of parental care evolution in monogamous mice. *Nature*, *544*(7651), 434–439. https://doi.org/10.1038/nature22074

Burkett, J. P., Andari, E., Johnson, Z. v., Curry, D. C., de Waal, F. B. M., & Young, L. J. (2016). Oxytocin-dependent consolation behavior in rodents. *Science*, *351*(6271), 375–378. https://doi.org/10.1126/science.aac4785 This

Carter, C. S., DeVries, A. C., & Getz, L. L. (1995). Physiological substrates of mammalian monogamy: the prairie vole model. *Neuroscience and Biobehavioral Reviews*, *19*(2), 303–314. http://www.ncbi.nlm.nih.gov/pubmed/7630584

Carter, C. S., Witt, D. M., Thompson, E. G., & Carlstead, K. (1988). Effects of hormonal, sexual, and social history on mating and pair bonding in prairie voles. *Physiology and Behavior*, *44*(6), 691–697. https://doi.org/10.1016/0031-9384(88)90049-2

Chen, J., Markowitz, J. E., Lilascharoen, V., Taylor, S., Sheurpukdi, P., Keller, J. A., Jensen, J. R., Lim, B. K., Datta, S. R., & Stowers, L. (2021). Flexible scaling and persistence of social vocal communication. *Nature*, *593*(7857), 108–113. https://doi.org/10.1038/s41586-021-03403-8

Coffey, K. R., Marx, R. G., & Neumaier, J. F. (2019). DeepSqueak: a deep learning-based system for detection and analysis of ultrasonic vocalizations. *Neuropsychopharmacology*, *44*(5), 859–868. https://doi.org/10.1038/s41386-018-0303-6

Coolen, L. M. (2005). Neural control of ejaculation. *Journal of Comparative Neurology*, *493*(1), 39–45. https://doi.org/10.1002/cne.20784

Cox, M. A. A., & Cox, T. F. (2008). Multidimensional Scaling. In C. Chen, W. Härdle, & A. Unwin (Eds.), *Handbook of Data Visualization* (pp. 315–347). Springer Berlin Heidelberg. https://doi.org/10.1007/978-3-540-33037-0_14

Curtis, J. T., & Wang, Z. (2003). Forebrain c-fos expression under conditions conducive to pair bonding in female prairie voles (Microtus ochrogaster). *Physiology & Behavior*, *80*, 95–101.

Cushing, B. S., Mogekwu, N., Le, W. W., Hoffman, G. E., & Carter, C. S. (2003). Cohabitation induced Fos immunoreactivity in the monogamous prairie vole. *Brain Research*, *965*, 203–211. https://doi.org/10.1016/S0006-8993(02)04199-9

Cushing, B. S., & Wynne-Edwards, K. E. (2006). Estrogen receptor-α distribution in male rodents is associated with social organization. *Journal of Comparative Neurology*, *494*(4), 595–605. https://doi.org/10.1002/cne.20826

de Vries, G. J. (2004). Minireview: Sex differences in adult and developing brains: Compensation, compensation, compensation. *Endocrinology*, *145*(3), 1063–1068. https://doi.org/10.1210/en.2003-1504

DeVries, A. C., & Carter, C. S. (1999). Sex differences in temporal parameters of partner preference in prairie voles (Microtus ochrogaster). *Canadian Journal of Zoology*, *77*, 885–889. https://doi.org/10.1139/cjz-77-6-885

Dewsbury, D. A. (1988). Copulatory behavior as courtship communication. *Ethology*, *79*, 218–234. https://doi.org/10.1111/j.1439-0310.1988.tb00712.x

Dong, H. W. (2008). The Allen reference atlas: A digital color brain atlas of the C57Bl/6J male mouse. In *The Allen reference atlas: A digital color brain atlas of the C57Bl/6J male mouse.* John Wiley & Sons Inc.

Eberhard, W. G. (1996). *Female control: Sexual selection by cryptic female choice*. Princeton University Press.

Emlen, S. T., & Oring, L. W. (1977). Ecology, sexual selection, and the evolution of mating systems. *Science*, *197*(4300), 215–223.

Ferguson, J. N., Aldag, J. M., Insel, T. R., & Young, L. J. (2001). Oxytocin in the medial amygdala is essential for social recognition in the mouse. *The Journal of Neuroscience*, *21*, 8278–8285.

Friard, O., & Gamba, M. (2016). BORIS: A free, versatile open-source event-logging software for video/audio coding and live observations. *Methods in Ecology and Evolution*, *7*(11), 1325–1330. https://doi.org/10.1111/2041-210X.12584

Georgiadis, J. R., Kringelbach, M. L., & Pfaus, J. G. (2012). Sex for fun: A synthesis of human and animal neurobiology. *Nature Reviews Urology*, *9*(9), 486–498. https://doi.org/10.1038/nrurol.2012.151

Getz, L. L., McGuire, B., Pizzuto, T., Hofmann, J. E., & Frase, B. (1993). Social organization of the prairie vole (Microtus ochrogaster). *Journal of Mammalogy*, *74*(1), 44–58.

González, I., Déjean, S., Pascal, M., & Alain, B. (2008). CCA: An R package to extend canonical correlation. *Journal of Statistical Software*, *23*(12), 1–14.

Hasson, U., Ghazanfar, A. A., Galantucci, B., Garrod, S., & Keysers, C. (2012). Brain-to-brain coupling: A mechanism for creating and sharing a social world. *Trends in Cognitive Sciences*, *16*, 114–121. https://doi.org/10.1016/j.tics.2011.12.007

Hawkley, L. C., & Cacioppo, J. T. (2010). Loneliness matters: A theoretical and empirical review of consequences and mechanisms. *Annals of Behavioral Medicine*, *40*(2), 218–227. https://doi.org/10.1007/s12160-010-9210-8

Hochberg, Y. (2015). Controlling the false discovery rate : a practical and powerful approach to multiple testing. *Journal of the Royal Statistical Society. Series B*, *57*(1), 289–300.

Horie, K., Inoue, K., Nishimori, K., & Young, L. J. (2020). Investigation of Oxtr-expressing neurons projecting to nucleus accumbens using Oxtr-ires-Cre knock-in prairie voles

(Microtus ochrogaster). *Neuroscience*, *448*, 312–324. https://doi.org/10.1016/j.neuroscience.2020.08.023

Hu, R. K., Zuo, Y., Ly, T., Wang, J., Meera, P., Wu, Y. E., & Hong, W. (2021). An amygdala-to-hypothalamus circuit for social reward. *Nature Neuroscience*, *24*(6), 831–842. https://doi.org/10.1038/s41593-021-00828-2

Insel, T. R., & Young, L. J. (2001). The neurobiology of attachment. *Nature Reviews Neuroscience*, *2*, 129–136. https://doi.org/10.1038/35053579

Kenkel, W. M., Gustison, M. L., & Beery, A. K. (2021). A neuroscientist's guide to the vole. *Current Protocols*, *1*, e175. https://doi.org/10.1002/cpz1.175

Kim, Y., Perova, Z., Mirrione, M. M., Pradhan, K., Henn, F. A., Shea, S., Osten, P., & Li, B. (2016). Whole-brain mapping of neuronal activity in the learned helplessness model of depression. *Frontiers in Neural Circuits*, *10*(February), 1–11. https://doi.org/10.3389/fncir.2016.00003

Kim, Y., Venkataraju, K. U., Pradhan, K., Mende, C., Taranda, J., Turaga, S. C., Arganda-Carreras, I., Ng, L., Hawrylycz, M. J., Rockland, K. S., Seung, H. S., & Osten, P. (2015). Mapping social behavior-induced brain activation at cellular resolution in the mouse. *Cell Reports*, *10*, 292–305. https://doi.org/10.1016/j.celrep.2014.12.014

Kim, Y., Yang, G. R., Pradhan, K., Venkataraju, K. U., Bota, M., Garcia del Molino, L. C., Fitzgerald, G., Ram, K., He, M., Levine, J. M., Mitra, P., Huang, Z. J., Wang, X., & Osten, P. (2017). Brain-wide map reveal stereotyped cell type-based cortical architecture and subcortical sexual dimorphism. *Cell*, *171*(2), 456–469. https://doi.org/doi:10.1016/j.cell.2017.09.020

Kingsbury, L., Huang, S., Wang, J., Gu, K., Golshani, P., Wu, Y. E., & Hong, W. (2019). Correlated neural activity and encoding of behavior across brains of socially interacting animals. *Cell*, *178*(2), 429-446.e16. https://doi.org/10.1016/j.cell.2019.05.022

Kinreich, S., Djalovski, A., Kraus, L., Louzoun, Y., & Feldman, R. (2017). Brain-to-brain synchrony during naturalistic social interactions. *Scientific Reports*, *7*(1), 1–12. https://doi.org/10.1038/s41598-017-17339-5

Knox, J., Harris, K. D., Graddis, N., Whitesell, J. D., Zeng, H., Harris, J. A., Shea-Brown, E., & Mihalas, S. (2019). High-resolution data-drive model of the mouse connectome. *Network Neuroscience*, *3*(1), 217–236. https://doi.org/10.1162/netn_a_00066

Lei, K., Cushing, B. S., Musatov, S., Ogawa, S., & Kramer, K. M. (2010). Estrogen receptor-α in the bed nucleus of the stria terminalis regulates social affiliation in male prairie voles (Microtus ochrogaster). *PLoS ONE*, *5*(1), 1–5. https://doi.org/10.1371/journal.pone.0008931

Lieberwirth, C., & Wang, Z. (2014). Social bonding: Regulation by neuropeptides. *Frontiers in Neuroscience*, *8*, 171. https://doi.org/10.3389/fnins.2014.00171

Long, M., Verbeke, W., Ein-Dor, T., & Vrtička, P. (2020). A functional neuro-anatomical model of human attachment (NAMA): Insights from first- and second-person social neuroscience. *Cortex*, *126*, 281–321. https://doi.org/10.1016/j.cortex.2020.01.010

López-Gutiérrez, M. F., Gracia-Tabuenca, Z., Ortiz, J. J., Camacho, F. J., Young, L. J., Paredes, R. G., Díaz, N. F., Portillo, W., & Alcauter, S. (2021). Brain functional networks associated with social bonding in monogamous voles. *ELife*, *10*, 1–25. https://doi.org/10.7554/ELIFE.55081

Marlowe, F. (2000). Paternal investment and the human mating system. *Behavioural Processes*, *51*, 45–61. https://doi.org/10.1016/S0376-6357(00)00118-2

Millard, S. P. (2013). *EnvStats: An R package for Environmental Statistics*. Springer.

Muñoz-Castañeda, R., Zingg, B., Matho, K. S., Chen, X., Wang, Q., Foster, N. N., Li, A., Narasimhan, A., Hirokawa, K. E., Huo, B., Bannerjee, S., Korobkova, L., Park, C. S., Park, Y. G., Bienkowski, M. S., Chon, U., Wheeler, D. W., Li, X., Wang, Y., … Dong, H. W. (2021). Cellular anatomy of the mouse primary motor cortex. *Nature*, *598*(7879), 159–166. https://doi.org/10.1038/s41586-021-03970-w

Murtagh, F., & Legendre, P. (2014). Ward's hierarchical agglomerative clustering method: Which algorithms implement Ward's criterion? *Journal of Classification*, *31*, 274–295. https://doi.org/10.1007/s00357-014-9161-z

Nieh, E. H., Vander Weele, C. M., Matthews, G. A., Presbrey, K. N., Wichmann, R., Leppla, C. A., Izadmehr, E. M., & Tye, K. M. (2016). Inhibitory input from the lateral hypothalamus to the ventral tegmental area disinhibits dopamine neurons and promotes behavioral activation. *Neuron*, *90*(6), 1286–1298. https://doi.org/10.1016/j.neuron.2016.04.035

Petzold, A., van den Munkhof, H. E., Figge-Schlensok, R., & Korotkova, T. (2023). Complementary lateral hypothalamic populations resist hunger pressure to balance nutritional and social needs. *Cell Metabolism*, *35*, 456–471. https://doi.org/10.1016/j.cmet.2023.02.008

Pfaus, J. G. (2009). Pathways of sexual desire. *The Journal of Sexual Medicine*, *6*(6), 1506–1533. https://doi.org/10.1111/j.1743-6109.2009.01309.x

Pfaus, J. G., & Heeb, M. M. (1997). Implications of immediate-early gene induction in the brain following sexual stimulation of female and male rodents. *Brain Research Bulletin*, *44*, 397–407.

Pfaus, J. G., Kippin, T. E., & Centeno, S. (2001). Conditioning and sexual behavior: A review. *Hormones and Behavior*, *40*, 291–321. https://doi.org/10.1006/hbeh.2001.1686\nS0018-506X(01)91686-1 [pii]

R Development Core Team. (2016). *R: A language and environment for statistical computing*. R Foundation for Statistical Computing. http://www.r-project.org/

Ragan, T., Kadiri, L. R., Venkataraju, K. U., Bahlmann, K., Sutin, J., Taranda, J., Arganda-Carreras, I., Kim, Y., Seung, H. S., & Osten, P. (2012). Serial two-photon tomography for automated ex vivo mouse brain imaging. *Nature Methods*, *9*(3), 255–258. https://doi.org/10.1038/nmeth.1854

Renier, N., Adams, E. L., Kirst, C., Wu, Z., Azevedo, R., Kohl, J., Autry, A. E., Kadiri, L., Umadevi Venkataraju, K., Zhou, Y., Wang, V. X., Tang, C. Y., Olsen, O., Dulac, C., Osten, P., & Tessier-Lavigne, M. (2016). Mapping of brain activity by automated volume analysis of immediate early genes. *Cell*, *165*(7), 1789–1802. https://doi.org/10.1016/j.cell.2016.05.007

Renier, N., Wu, Z., Simon, D. J., Yang, J., Ariel, P., & Tessier-Lavigne, M. (2014). IDISCO: A simple, rapid method to immunolabel large tissue samples for volume imaging. *Cell*, *159*, 896–910. https://doi.org/10.1016/j.cell.2014.10.010

Scribner, J. L., Vance, E. A., Protter, D. S. W., Sheeran, W. M., Saslow, E., Cameron, R. T., Klein, E. M., Jimenez, J. C., Kheirbek, M. A., & Donaldson, Z. R. (2020). A neuronal signature for monogamous reunion. *Proceedings of the National Academy of Sciences*, *117*(20), 11076–11084. https://doi.org/10.1073/pnas.1917287117

Sheng, M., & Greenberg, M. E. (1990). The regulation and function of c-fos and other immediate early genes in the nervous system. *Neuron*, *4*, 477–485. https://doi.org/10.1016/0896-6273(90)90106-P

Snyder-Mackler, N., Burger, J. R., Gaydosh, L., Belsky, D. W., Noppert, G. A., Campos, F. A., Bartolomucci, A., Yang, Y. C., Aiello, A. E., O'Rand, A., Harris, K. M., Shively, C. A.,

Alberts, S. C., & Tung, J. (2020). Social determinants of health and survival in humans and other animals. *Science (New York, N.Y.)*, *368*(6493). https://doi.org/10.1126/science.aax9553

Trivers, R. L. (1972). Parental investment and sexual selection. In B. Campbell (Ed.), *Sexual Selection and the Descent of Man* (pp. 136–179). Aldine.

Uy, F. M. K., Jernigan, C. M., Zaba, N. C., Mehrotra, E., Miller, S. E., & Sheehan, M. J. (2021). Dynamic neurogenomic responses to social interactions and dominance outcomes in female paper wasps. *PLoS Genetics*, *17*(9), 1–25. https://doi.org/10.1371/journal.pgen.1009474

Veening, J. G., & Coolen, L. M. (2014). Neural mechanisms of sexual behavior in the male rat: Emphasis on ejaculation-related circuits. *Pharmacology Biochemistry and Behavior*, *121*, 170–183. https://doi.org/10.1016/j.pbb.2013.12.017

Veening, J. G., Coolen, L. M., & Gerrits, P. O. (2014). Neural mechanisms of female sexual behavior in the rat; Comparison with male ejaculatory control. *Pharmacology Biochemistry and Behavior*, *121*, 16–30. https://doi.org/10.1016/j.pbb.2013.11.025

Vu, T. D., Iwasaki, Y., Shigenobu, S., Maruko, A., Oshima, K., Iioka, E., Huang, C. L., Abe, T., Tamaki, S., Lin, Y. W., Chen, C. K., Lu, M. Y., Hojo, M., Wang, H. V., Tzeng, S. F., Huang, H. J., Kanai, A., Gojobori, T., Chiang, T. Y., … Okada, N. (2020). Behavioral and brain-transcriptomic synchronization between the two opponents of a fighting pair of the fish Betta splendens. *PLoS Genetics*, *16*(6), 1–29. https://doi.org/10.1371/journal.pgen.1008831

Walum, H., & Young, L. J. (2018). The neural mechanisms and circuitry of the pair bond. *Nature Reviews Neuroscience*, *19*(11), 643–654. https://doi.org/10.1038/s41583-018-0072-6

Wang, H. T., Smallwood, J., Mourao-Miranda, J., Xia, C. H., Satterthwaite, T. D., Bassett, D. S., & Bzdok, D. (2020). Finding the needle in a high-dimensional haystack: Canonical correlation analysis for neuroscientists. *NeuroImage*, *216*(December 2019), 116745. https://doi.org/10.1016/j.neuroimage.2020.116745

Williams, J. R., Catania, K. C., & Carter, C. S. (1992). Development of partner preferences in female prairie voles (Microtus ochrogaster): the role of social and sexual experience. *Hormones and Behavior*, *26*(3), 339-49.

Wu, Y. E., Dang, J., Kingsbury, L., Zhang, M., Sun, F., Hu, R. K., & Hong, W. (2021). Neural control of affiliative touch in prosocial interaction. *Nature*, *599*(7884), 262–267. https://doi.org/10.1038/s41586-021-03962-w

Yee, J. R., Kenkel, W. M., Kulkarni, P., Moore, K., Perkeybile, A. M., Toddes, S., Amacker, J. A., Carter, C. S., & Ferris, C. F. (2016). BOLD fMRI in awake prairie voles: A platform for translational social and affective neuroscience. *NeuroImage*, *138*, 221–232. https://doi.org/10.1016/j.neuroimage.2016.05.046

Young, K. A., Gobrogge, K. L., Liu, Y., & Wang, Z. (2011). The neurobiology of pair bonding: Insights from a socially monogamous rodent. *Frontiers in Neuroendocrinology*, *32*(1), 53–69. https://doi.org/10.1016/j.yfrne.2010.07.006

Young, L. J., & Wang, Z. (2004). The neurobiology of pair bonding. In *Nature Neuroscience* (Vol. 7, Issue 10, pp. 1048–1054). Nature Publishing Group. https://doi.org/10.1038/nn1327

Zhang, W., & Yartsev, M. M. (2019). Correlated neural activity across the brains of socially interacting bats. *Cell*, *178*(2), 413-428.e22. https://doi.org/10.1016/j.cell.2019.05.023

Supplementary information

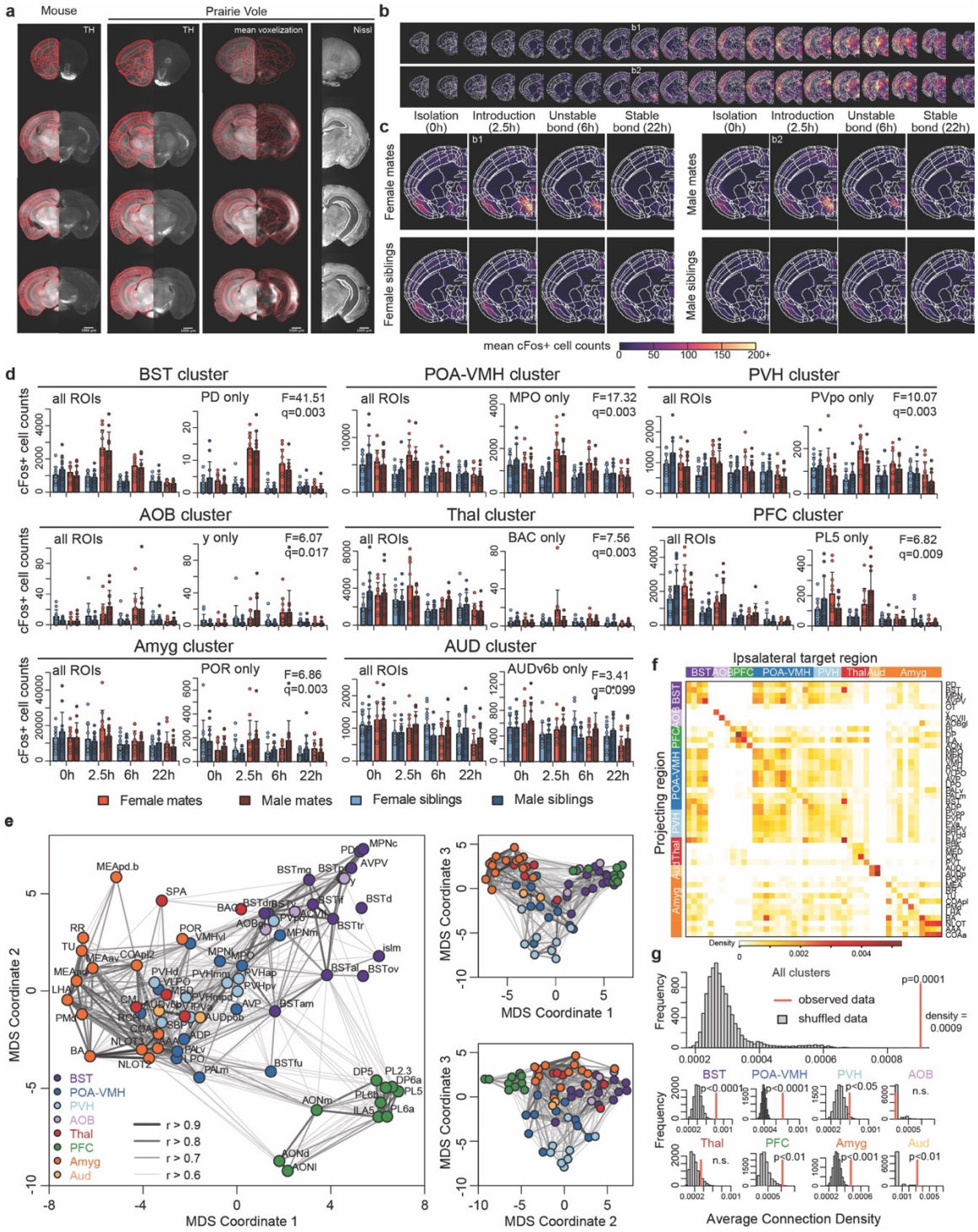

Figure Supplement 1. Validation of the prairie vole reference atlas and brain-wide patterns of immediate early gene expression during pairing. a. Mouse (left panel). Coronal sections composition of mouse reference brain overlay with atlas boundaries in red (left) and the same

964 section of TH immunolabeling (right). Prairie vole (left column). Similar coronal brain sections
965 of prairie vole reference brain and atlas boundaries in red (left) with TH immunolabeling (right).
966 (center column) Same coronal section of prairie vole reference brain and c-Fos+ mean
967 voxelization overlay with atlas boundaries in red. (left column) Same coronal sections of prairie
968 vole NeuroTrace staining registered onto prairie vole reference brain. **b.** Coronal cross-sections
969 (rostral to caudal) from female (top) and male (bottom) mating pairs are shown for the 2.5h
970 timepoint group, with brightness corresponding to the average voxel c-Fos+ cell counts. **c.** A
971 representative coronal slice that includes posterior BST is shown for mate pairs and siblings and
972 separated by timepoint and sex. Brightness corresponds to average voxel c-Fos+ cell counts per
973 group. **d.** Counts of c-Fos+ cells are shown for ROIs associated with pair-bond development,
974 organized by hierarchal cluster. For each cluster, the total counts are shown on the right and the
975 most significant ROI (highest F-statistic) is shown on the right. Counts are summarized by
976 timepoint, partner type and sex (mean ± sd), and overlaid with counts from individual animals.
977 Mate pairs are in red and sibling pairs in blue (female in lighter hues, males in darker hues). Test
978 statistics are from an ANOVA to compare null and hypothesized general linear models. FDR q-
979 values are from permutation tests to assess the likelihood of the observed test statistic as
980 compared to a distribution of test statistics obtained from shuffled data. **e.** Representations of the
981 first three dimensions of a multi-dimensional scaling (MDS) coordinate space based on Pearson
982 correlations between c-Fos+ cell counts in brain regions (ROIs) associated with bonding. Each
983 symbol represents an ROI and is colored based on cluster assignment. Darkness and thickness of
984 connecting lines reflect correlation coefficients. **f.** This heatmap shows normalized connection
985 densities (Knox et al., 2019) from projecting to ipsilateral target ROIs in the mouse brain. These
986 ROIs are the same as, or larger divisions that contain, the ROIs found to be associated with pair-
987 bond development in our analysis. **g.** The top histogram shows results of a permutation test to
988 assess whether hierarchical clusters of chosen ROIs in our analysis mirror underlying anatomical
989 connections. Observed connectivity reflects the overall average of cluster means, which is
990 compared to averages from 10,000 iterations of shuffled data (i.e., target regions shuffled for
991 each projecting region). The bottom histograms show the results of permutation tests for the
992 mean connectivity within each cluster of ROIs.

993

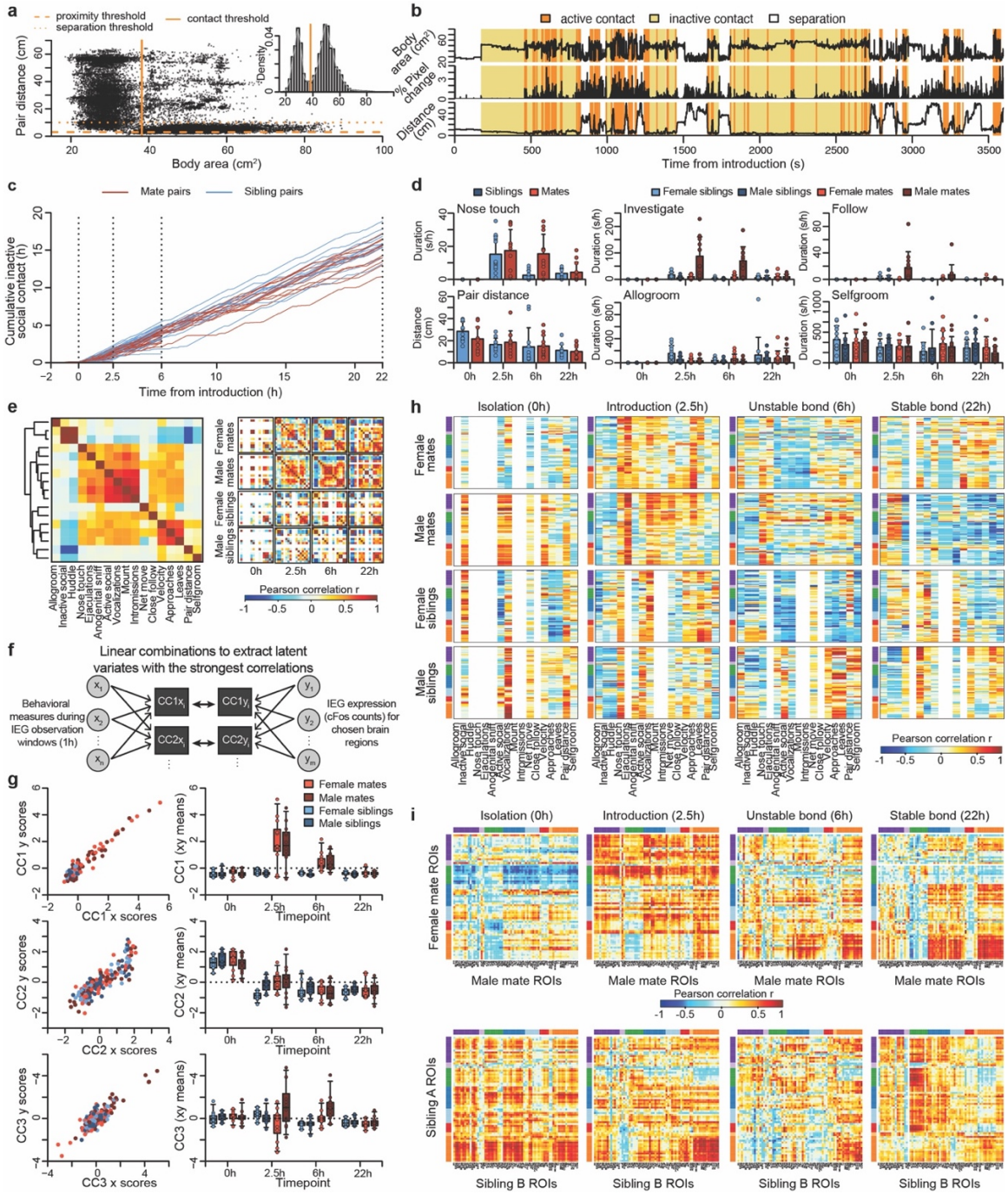

994

995 **Figure Supplement 2. Behavioral phenotypes during pairing and patterns of associate**
996 **between brain-wide immediate early gene expression and behavior. a.** Long-term tracking of
997 social states was informed by automated measures of the largest body area, pair activity, and pair
998 distance. On the left, body area is plotted against dyad distance from an exemplar 24h mate pair
999 video (10% randomly selected frames from 12 hours of white light). On the right, the density
1000 curve for body area reveals a basic threshold for when animals are separated or in physical

contact. **b.** Traces of body area, video activity, and pair distance are plot for the first hour of interaction of the exemplar mate pair, along with automated assignments of behavioral states. **c.** Cumulative time spent in inactive social contact for up to 22h of cohabitation in mate pairs (red lines) and sibling pairs (blue lines). **d.** Group differences (mean ± sd) are shown for appetitive behaviors including nose-to-nose touching, anogenital investigation, and close follows. Group differences (mean ± sd) are shown for proximity and grooming behaviors including pair distance, allogrooming, and selfgrooming. Mate pairs are in red and sibling pairs in blue (female in lighter hues, males in darker hues). T-tests were used to compare mates and siblings, and paired t-tests were used to compare female and male mates. **e.** Hierarchical clustering of behavioral measures from Pearson correlations groups behavioral states and interactions into three main clusters involving close contact (e.g., huddling and allogrooming), mating (e.g., mounts, vocalizations), and appetitive behavior (e.g., approaches and follows). On the right, Pearson correlations are shown among behaviors in subsets based on partner type, sex, and timepoint. Warm and cool colors indicate positive and negative correlation coefficients, respectively. White indicates behaviors with no variation, meaning that coefficients were not computed (e.g., siblings did not exhibit mating behaviors). **f.** Schematic of canonical correlation analysis (CCA), where two sets of variables (x and y) are combined linearly to extract latent variates with the strongest correlations (CC1 stronger than CC2, and so on). This analysis outputs x and y scores for each latent variate for each animal subject in the dataset. In this dataset, x scores represent linear combinations of behavioral measures, and y scores represent linear combinations of ROI c-Fos counts. **g.** On the left, the relationship between x and y scores is shown for all study animals for the first three variates. On the right, the means of x and y scores for the first three variates are compared across partner type, sex, and timepoint (boxplots = median, 25%-75% quartile, and 95% confidence intervals). **h.** Heatmaps represent Pearson correlation coefficients, with brain regions on the y-axis (grouped into hierarchical clusters, see Figure 3 for ROI and cluster labels) and behavioral outcomes (during 1h observation windows) on the x-axis. Correlation heatmaps are split by partner type, sex and timepoint. Warm and cool colors indicate positive and negative correlation coefficients, respectively. White indicates behaviors with no variation, meaning that coefficients were not computed (e.g., siblings did not exhibit mating behaviors). **i.** On the top, heatmaps represent Pearson correlation coefficients between selected brain regions (ROIs) in mating pairs, with female data on the y-axis and male data on the x-axis. On the bottom,

heatmaps represent Pearson correlation coefficients between selected ROIs in sibling dyads, where sibling A data are from animals placed in the left side of chamber during isolation, and sibling B data are from animals placed on the right side. ROIs are grouped by hierarchical clustering (see Figure 3). Warm and cool colors indicate positive and negative correlation coefficients, respectively.

Supplemental File 1. Statistical comparisons of absolute and relative brain area volumes between prairie voles and mice. Absolute and relative area volumes (normalized to total brain volume) are compared between prairie voles and male mice. Absolute brain area volumes are all statistically significant bigger in the prairie vole compared to the mouse, but none the ratios of area volume (relative to the whole brain) were statistically different between species. Mean, SD, p-values, and FDR correction of the p-values are presented for each region.

Supplemental File 2 (separate file). Statistical comparisons of absolute and relative brain area volumes between male and female prairie voles. Absolute and relative area volumes (normalized to total brain volume) are compared between male and female prairie voles. No statistical differences were found in these sex comparisons. Mean, SD, p-values, and FDR correction of the p-values are presented for each region.

Supplemental File 3 (separate file). Behavior ethogram. Descriptions of automated, semi-automated, and manually scored behavioral measures.

Video 1. Prairie vole reference brain. The prairie vole reference brain from LSFM imaging is shown from coronal cross-sections (rostral to caudal) and in a 3D view. Then, coronal cross-sections are show of the prairie vole atlas (left) alongside whole-brain staining for somatostatin (SST, middle) and fluorescent Nissl (NeuroTrace, right).

1058

1059 **Video 2. Patterns of whole-brain immediate early gene expression during pairing.** First,
1060 coronal cross-sections of average IEG induction patterns are shown for female (first video) and
1061 male (second video) prairie voles across each of the 16 experiment groups split by partner type
1062 (mates-top, siblings-bottom) and timepoint (0, 2.5, 6, 22 hours from left to right). Brightness
1063 corresponds to average voxel c-Fos+ cell counts. These videos are associated with Figure
1064 Supplement 1b,c (see these panels for the color key). The induction patterns are overlaid with
1065 prairie vole atlas boundaries. Next, coronal cross-sections are shown with the results of model
1066 comparisons to identify brain areas associated with bonding. This video is associated with Figure
1067 3A (see this panel for the color key). The reference is overlaid with colored voxels that represent
1068 a difference (FDR $q < 0.1$) between hypothesized general linear model that included partner type
1069 and a null model that did not. Warm colors indicate voxels with higher c-Fos+ counts in mate
1070 pairs (test statistic for partner type > 0), and cooler colors indicate voxels with higher c-Fos+ cell
1071 counts in siblings (test statistic for partner type < 0). Finally, coronal cross-sections are shown
1072 with the results of model comparisons to identify brain areas associated with sex differences. The
1073 reference is overlaid with colored voxels that represent a difference (FDR $q < 0.1$) between
1074 hypothesized general linear model that included a partner type x sex interaction term and a null
1075 model that did not. Colored voxels indicate regions where there was an interaction effect, with
1076 warm colors indicating a positive interaction term and cool colors indicating a negative
1077 interaction term (see Figure 3A color key).